PHYSICAL REVIEW B **92**, 184420 (2015)

Optical hyperpolarization of ^{13}C nuclear spins in nanodiamond ensembles

Q. Chen,[1,2] I. Schwarz,[1,2] F. Jelezko,[2,3] A. Retzker,[4] and M. B. Plenio[1,2]
[1]*Institut für Theoretische Physik, Albert-Einstein-Allee 11, Universität Ulm, 89069 Ulm, Germany*
[2]*IQST, Albert-Einstein-Allee 11, Universität Ulm, 89069 Ulm, Germany*
[3]*Institut für Quantenoptik, Universität Ulm, 89073 Ulm, Germany*
[4]*Racah Institute of Physics, The Hebrew University of Jerusalem, Jerusalem 91904, Israel*
(Received 8 June 2015; revised manuscript received 8 September 2015; published 18 November 2015)

Dynamical nuclear polarization holds the key for orders of magnitude enhancements of nuclear magnetic resonance signals which, in turn, would enable a wide range of novel applications in biomedical sciences. However, current implementations of DNP require cryogenic temperatures and long times for achieving high polarization. Here we propose and analyze in detail protocols that can achieve rapid hyperpolarization of ^{13}C nuclear spins in randomly oriented ensembles of nanodiamonds at room temperature. Our protocols exploit a combination of optical polarization of electron spins in nitrogen-vacancy centers and the transfer of this polarization to ^{13}C nuclei by means of microwave control to overcome the severe challenges that are posed by the random orientation of the nanodiamonds and their nitrogen-vacancy centers. Specifically, these random orientations result in exceedingly large energy variations of the electron spin levels that render the polarization and coherent control of the nitrogen-vacancy center electron spins as well as the control of their coherent interaction with the surrounding ^{13}C nuclear spins highly inefficient. We address these challenges by a combination of an off-resonant microwave double resonance scheme in conjunction with a realization of the integrated solid effect which, together with adiabatic rotations of external magnetic fields or rotations of nanodiamonds, leads to a protocol that achieves high levels of hyperpolarization of the entire nuclear-spin bath in a randomly oriented ensemble of nanodiamonds even at room temperature. This hyperpolarization together with the long nuclear-spin polarization lifetimes in nanodiamonds and the relatively high density of ^{13}C nuclei has the potential to result in a major signal enhancement in ^{13}C nuclear magnetic resonance imaging and suggests functionalized and hyperpolarized nanodiamonds as a unique probe for molecular imaging both *in vitro* and *in vivo*.

DOI: 10.1103/PhysRevB.92.184420 PACS number(s): 76.70.Fz, 03.67.Lx, 67.30.hj, 76.90.+d

I. INTRODUCTION

Nuclear magnetic resonance (NMR) [1,2] and magnetic resonance imaging (MRI) [3] have evolved to be powerful techniques to extract molecular-level information in a wide variety of physical, chemical, and biological applications. Recently, ^{13}C based MRI has emerged as a platform enabling essentially background-free imaging of nonproton nuclei with the additional possibility for the local and permanent destruction of the signal by means of radio frequency (rf) pulses [4]. However, the low signal-to-noise ratio for ^{13}C based MRI is not sufficient for most clinical and research applications due to the combination of a relatively low gyromagnetic ratio of ^{13}C and of the low natural abundance of this nucleus. Several strategies have been proposed to enhance the sensitivity of ^{13}C based MRI. Particularly promising in this context is the hyperpolarization of the ^{13}C nuclei, i.e., the generating of a large, nonthermal ^{13}C nuclear-spin polarization. Indeed, hyperpolarized ^{13}C based MRI has shown exciting potential for *in vivo* applications, especially for metabolic imaging [5–7]. One of the most powerful methods for the generation of hyperpolarization is dynamic nuclear polarization (DNP) [8–12], in which a large polarization of electron spins is transferred to nuclear spins, resulting in an enhancement of the MRI signal by several orders of magnitude.

Over the last decade, several breakthroughs have occurred in the manufacturing, surface treatment, and use of nanoparticles for biomedical applications [13]. Biocompatible nanoparticles present an attractive platform for hyperpolarization, as they can be functionalized for molecular specificity, can exhibit long nuclear-spin-relaxation times, and contain numerous nuclear spins of a single species (e.g., carbon). Long-lived hyperpolarization has been demonstrated in silica nanoparticles [14] and nanodiamonds [15,16], using standard DNP protocols, i.e., transferring the high thermal electron spin polarization at cryogenic temperatures in a strong external magnetic field to nuclei. Nanodiamonds in particular offer exciting possibilities as novel hyperpolarized probes. In addition to excellent biocompatibility [17], the possibility for surface functionalization and nuclear-spin-relaxation time of several minutes [18], nanodiamonds contain crystal point defects with unique optical and magnetic properties. Amongst these the negatively charged nitrogen-vacancy (NV) center stands out as its electron spin can be polarized over 95% within microseconds by optical pumping while exhibiting a relaxation time in the millisecond range even at room temperature [19]. In combination with the ability for transferring this near perfect electron-spin polarization to surrounding nuclear spins by means of microwave radiation, nanodiamond optical DNP promises to overcome the severe limitations on the maximally achievable polarization at room temperature by currently available methods. This would establish the NV center electron spin as a promising candidate for achieving nanodiamond hyperpolarization at ambient conditions—room-temperature optical DNP.

Previous work has demonstrated that in bulk diamond electron-spin polarization of the NV center can be generated and subsequently be transferred via hyperfine interactions to nearby nuclei. This polarization can then be detected indirectly via the NV center [15,20–27] or directly via an NMR scanner

[28]. To this end, in bulk diamonds a high magnetic field is aligned with the natural quantization axis of the NV center to enable optical pumping to a specific electron-spin state. Controlled interaction of the electron spin with specific nearby nuclear-spins species can then be achieved for example by the application of continuous-wave microwave (MW) radiation applied to the NV center electron spin [24]. When the Rabi frequency of the microwave driving field matches the Larmor frequency of a specific nuclear-spin species [achieving a Hartmann-Hahn (HH) resonance [29]], flip-flops can occur between the microwave dressed states of the electron spin of the NV center and the surrounding ^{13}C nuclear spins [30–32] as was recently demonstrated experimentally [24].

However, medical MRI applications require large ensembles of nanodiamonds. In such ensembles (powder or solution) the angle between the external magnetic field and the orientation of NV centers and therefore their natural quantization axis is randomly distributed. This brings about several challenges for achieving high levels of hyperpolarization that need to be addressed by means of carefully designed protocols. First, the energy levels of the NV spin are then distributed over a large energy range of possible values so that the applied microwave field will be resonantly coupled to an exceedingly small fraction of the NV spins. Second, in an external magnetic field, additional limitations concern the optical polarization of the NV spins. In particular, the NV spins will be initialized to different states relative to the laboratory frame depending on their angle with the external magnetic field, thus resulting in a small net polarization.

In this work we show how to address these challenges to achieve a radical enhancement of the hyperpolarization in a nanodiamond ensemble. To this end we use an off-resonant driving and the integrated solid effect (ISE) for the NV center spin, resulting in a robust spin-polarization transfer between the NV and nuclear spins. A very large fraction of the NV electron spins can be coherently coupled to neighboring nuclear spins. Additionally, adiabatic rotation of the magnetic fields, or the Brownian rotation of the nanodiamonds themselves (in powder or solution respectively), is proposed for extending the polarization scheme to almost the entire nanodiamond ensemble. We also discuss the effect of spin diffusion induced by the nuclear dipole-diploe interactions which will further support the polarization of large volumes.

It should be noted that the principles of optical DNP that we develop in this work can be transferred to any color center that possesses an electron spin in the ground state and admits optical pumping of this electron spin. The paper is organized as follows. In Sec. II we present the coherent coupling and polarization of a single nuclear spin near a randomly oriented NV spin. This serves the introduction of the principal challenges in nanodiamond ensemble polarization, the discussion of the robust initialization and construction of suitable dressed states for the NV center electron spin, and the realization of near resonant coupling with the nuclear spin by using off-resonant driving and the integrated solid effect. In Sec. III, we introduce mechanisms to extend our polarization protocols to the entire nanodiamond ensemble, both for nanodiamond powder and for nanodiamonds in a solution. In Sec. IV, we consider our protocol for multiple ^{13}C nuclear spins and include the effect of dipolar coupling among the nuclear spins and in particular the benefits of nuclear-spin diffusion. In Sec. V we demonstrate the applicability of our polarization schemes for another very broad range of NV center orientations. In Sec. VI we take into account the effect of depolarization processes on the efficiency of our polarization protocol. Finally, the discussion and conclusion parts are given in Secs. VII and VIII, respectively.

II. MAGNETIC MANIPULATION AND POLARIZATION OF A SINGLE NUCLEAR SPIN NEARBY A RANDOMLY ORIENTED NV SPIN

A. Difficulties from the random orientations

The nanodiamond ensembles that we are interested in are realized as powder or solutions. In both cases the spatial orientations of the nanodiamonds and therefore of the NV centers hosted in them is random and uniformly distributed across the full solid angle [see Fig. 1(a) for an illustration]. In the laboratory frame this leads to the lack of a common quantization axis for the NV centers. We begin by describing in more detail the two principal challenges that are being imposed by these random spatial orientations: (1) The direction of the natural quantization axis associated with the crystal-field

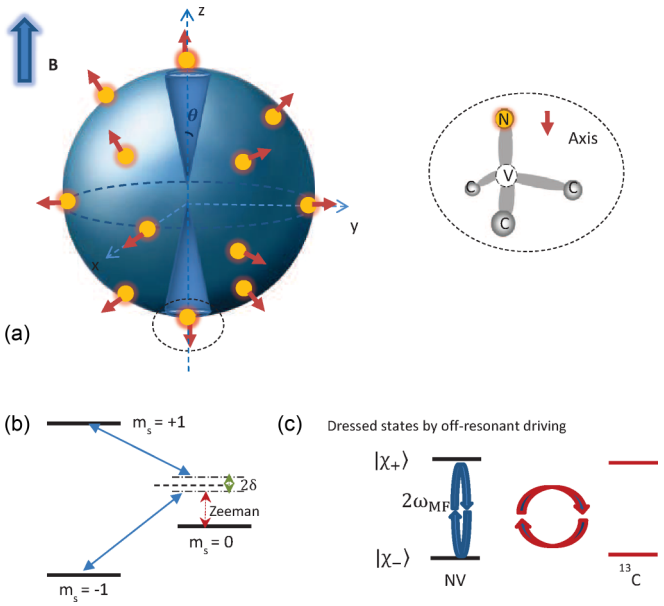

FIG. 1. (Color online) Schematic of dressed-state resonant coupling of NV spins and nuclear spins in a nanodiamond ensemble and energy-level diagrams. (a) The random orientations of the NV spins are uniformly distributed over the unit sphere. Small yellow circles represent examples with orientations indicated by red arrows which represent the unit vector pointing from the nitrogen to the vacancy of an NV center (see the example of such an NV center in the dashed circle, the axis pointing along "N-V" forms the natural quantisation axis). (b) Ground electronic spin states of an NV center in a strong external magnetic field. Microwave driving fields are applied off-resonantly achieving an effective resonant double quantum transition between the state $m_s = +1$ and $m_s = -1$ in the large detuning regime. (c) The effective coupling provides a dressed state basis which then permits energy conserving flip-flops between the dressed states and external resonant nuclear spins.

energy splitting D is not controllable, resulting in a significant variance of the energy levels in the presence of an external magnetic field, and (2) optical pumping of the NV center electron spins in an external magnetic field will not initialize all NV center electron spins to the same state.

1. Zero-field and external magnetic field distribution

The negatively charged NV center, in the following denoted for brevity as the NV center, realizes in its ground state an electronic spin triplet ($S = 1$) which exhibits a zero-field splitting of $D = (2\pi)2.87$ GHz which separates the $|m_s = 0\rangle$ state energetically from the degenerate $|m_s = \pm\rangle$ manifold. The application of an external magnetic field, in the following assumed to take the value $B = 0.36$ T, lifts this remaining degeneracy such that the state $m_s = -1$ is shifted below the $m_s = 0$ state [see Fig. 1(b)]. The zero-field splitting and the Zeemann effect due to an external magnetic field of the NV center are described by

$$H_{NV} = \vec{S}\mathbf{D}\vec{S} + \gamma_e \vec{B}\vec{S}. \tag{1}$$

Herein $\mathbf{D}$ denotes the orientation dependent zero-field splitting tensor, $\gamma_e = (2\pi)28.7$ GHz/T the gyromagnetic ratio, $\vec{S}$ the electron spin-1 vector operator [33], and $\vec{B}$ the magnetic field vector. In the principal axis system defined by the NV symmetry axes, the zero-field splitting tensor $\mathbf{D}$ is diagonal,

$$\mathbf{D} = \mathrm{diag}\left(-\tfrac{1}{3}D + E, -\tfrac{1}{3}D - E, \tfrac{2}{3}D\right). \tag{2}$$

Here E denotes the strain dependent contribution. It is worth emphasizing that in the scenario that we are considering here, the orientation of the symmetry axis of the NV center relative to the external magnetic field is uniformly distributed over the unit sphere. For the following it will be convenient to conduct the discussion in the laboratory frame whose z axis we define to take the direction of the externally applied strong magnetic field, $\gamma_e B \gg D$. In this frame, the zero-field splitting tensor $\mathbf{D}$ will have off-diagonal elements. As $\gamma_e B \gg D$ these off-diagonal elements are rapidly rotating so that their main effect will be energy shifts of the diagonal element of the Hamiltonian. The Hamiltonian can then be written as (see the Appendix for details of the derivation)

$$H''_{\mathrm{eff}} = [\gamma_e B + \delta(\theta)]S_z + D(\theta)S_z^2, \tag{3}$$

where

$$D(\theta) = \frac{D[1 + 3\cos(2\theta)] + 3E[1 - \cos(2\theta)]}{4},$$
$$\delta(\theta) = \frac{\gamma_e B|G_1|^2}{(\gamma_e B)^2 - [D(\theta)]^2} + \frac{|G_2|^2}{2\gamma_e B}, \tag{4}$$

θ is the angle between the magnetic field direction and the NV axis and the G_i are given in the Appendix. Clearly, the random orientations of the NV centers cause a variation of the zero-field splitting $D(\theta)$ across the entire interval $[-(2\pi)1.43$ GHz,$(2\pi)2.87$ GHz$]$ and $\delta(\theta)$ across the interval $[0$ MHz,$(2\pi)140$ MHz$]$ as shown in Fig. 2.

If we were to follow the scheme of Ref. [24], i.e., without the combination of off-resonant drive and ISE technique that we will present in this work, the uncertain detuning of the MW frequency from the electronic resonance can reach the order of GHz, which in turn would prevent effective polarization transfer.

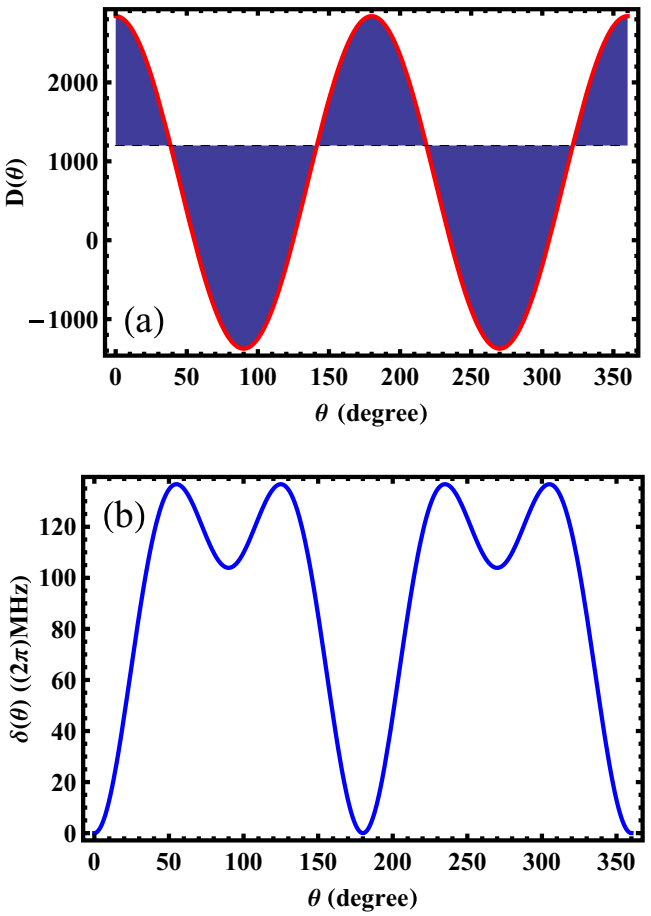

FIG. 2. (Color online) (a) Zero-field distribution $D(\theta)$ of the NV spins in nanodiamonds with $D = (2\pi)2.87$ GHz and $E = (2\pi)20$ MHz. (b) The second-order corrections which induce an energy distribution $\delta(\theta)$.

2. Optical initialization of NV spins at the high magnetic field limit

A second important difference between a randomly oriented nanodiamond ensemble and a bulk diamond concerns the optical polarization of electron spins of the NV center. For bulk diamonds, the magnetic field can be aligned with the principal axis of the NV center and the electronic spin of the NV center can be optically polarized to the state $|m_s = 0\rangle$ by illumination with a 532-nm green laser. However, for an ensemble of randomly oriented nanodiamonds, even in the limit of a strong magnetic field, the NV centers will be optically pumped to the state $|m_s = 0\rangle_\theta$ that is defined by the relative orientation of the NV center with respect to the externally applied magnetic field which defines the laboratory frame.

As discussed in the Appendix, these two coordinate systems can be transformed into each other and, employing $S_{z_\theta} = \cos\theta S_z - \sin\theta(\cos\phi S_x - \sin\phi S_y)$, we can express the eigenstate $|m_s = 0\rangle_\theta$ in terms of the eigenstates $|0\rangle, |\pm 1\rangle$ of

Eq. (3), i.e., in the laboratory frame, as

$$|0\rangle_\theta = \cos\theta|0\rangle + \frac{\sin\theta}{\sqrt{2}}(e^{i\phi}|+1\rangle - e^{-i\phi}|-1\rangle). \quad (5)$$

If θ is large, the eigenstate $|0\rangle$ of the NV center in the laboratory frame as given by Hamiltonian Eq. (3) differs significantly from the zero-field eigenstate $|0\rangle_\theta$ of the NV center. Hence optical initialization of randomly oriented NV centers lead to very different states depending on the orientation of the NV center.

Notice though that for moderate misalignment between the NV center orientation and external magnetic field, the initialization of the NV center is well approximated by $|0\rangle$. Indeed, for $\theta < 10^\circ$, $|\langle 0|0\rangle_\theta|^2 > 0.97$ and for $\theta < 20^\circ$ we find $|\langle 0|0\rangle_\theta|^2 > 0.88$ which implies significant polarization along the quantization axis defined by the external magnetic field. Therefore, for all the orientations of the NV centers that fall into two spherical sectors whose cone angle is 2θ, i.e., the two blue spherical sectors in Fig. 1(a), significant optical polarization can be achieved. From now on, we define a deviation by θ to imply that the symmetry axis of the NV spins falls within these two spherical cones.

B. The main ideas

The main idea that we will develop in this section consists of three main ingredients, namely (i) the generation of an energy gap between electronic states that is relatively robust with respect to variations in the relative orientation between the NV center and an external magnetic field, and at the same time (ii) a strong coupling between these electronic states and nuclear spins. Finally, (iii) the integrated solid effect is employed to achieve additional robustness against imperfections. All this is achieved by the use of dressed states in a ladder-type configuration in which the single quantum transitions are far detuned and the double quantum transition is nearly resonant (see Fig. 3).

In such a setting, that is for a detuning on the single quantum transition $D(\theta)$, the effective Rabi frequency and thus the energy splitting on the double quantum transition is proportional to $\Omega^2/D(\theta)$, in which Ω is related to the Rabi frequency of the applied microwave field and defined later. In leading order in θ, this suffers a variation that is of the order of $\Omega^2/D^2(\theta)\frac{\partial D(\theta)}{\partial\theta}\theta$. This contrasts with the case of the detuned driving single quantum transition only. In that case the effective energy gap is proportional to $\sqrt{D^2(\theta)+\Omega^2}$ which, if $D(\theta) \gg \Omega$, suffers a variation that is of order $\frac{\partial D(\theta)}{\partial\theta}\theta$. Therefore the variation in the former is suppressed by a factor of $\Omega^2/D^2(\theta)$ compared to the latter. This makes it much easier to achieve and maintain a Hartmann-Hahn resonance.

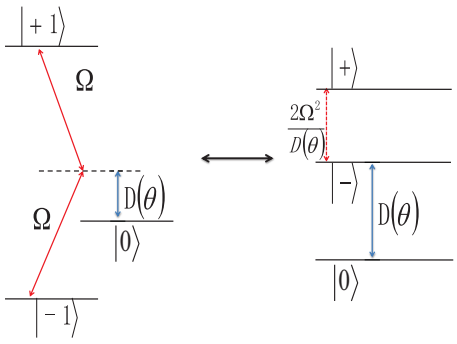

FIG. 3. (Color online) The level structure of the three-level Hartmann-Hann. A gap is created between the $|+\rangle = \frac{1}{\sqrt{2}}(|+1\rangle + |-1\rangle)$ and the $|-\rangle = \frac{1}{\sqrt{2}}(|+1\rangle - |-1\rangle)$ states. This gap is robust to changes in the one photon detuning $[D(\theta)]$ and is also robust to small changes in the two-photon detuning $[\delta(\theta)]$. Due to the fact that the coupling to the nuclei is via the dressed states $(|+\rangle, |-\rangle)$ and not the bare states, the coupling is not decreased due to the off resonant drivings.

The second crucial ingredient is related to the fact that the coupling between the electron spin and the nuclear spins is mediated by terms of the form $S_z \otimes I_z$. In a far-detuned single quantum transition the eigenstates involved in the Hartmann-Hahn resonance are $|m_s = 0\rangle + \frac{\Omega}{D(\theta)}|m_s = +1\rangle$ and $|m_s = +1\rangle - \frac{\Omega}{D(\theta)}|m_s = 0\rangle$. As these states are close to being eigenstates of S_z they hardly couple and in consequence the electron-nuclear coupling is suppressed by a factor proportional to $\frac{\Omega}{D(\theta)}$ when compared to the coupling between states with equally weighted superpositions $|m_s = 0\rangle \pm |m_s = +1\rangle$ which one would have obtained for resonant driving. Crucially, thanks to the small detuning on the double quantum transition we obtain $|m_s = -1\rangle \pm |m_s = +1\rangle$ which leads to a strong coupling between electron and nuclear spins if a Hartmann-Hahn resonance is realized (see right-hand side of Fig. 3). The latter is relatively robust thanks to the strong detuning on the single quantum transitions.

So far we have ignored additional energy shifts on the double quantum transition $\delta(\theta)$ which will lead to a loss of the Hartmann-Hahn resonance. In order to confer additional robustness to our scheme, rather than aiming to maintain a fixed Hartmann-Hahn resonance, we consider an adiabatic sweep of the external magnetic field on the double quantum transition where start and endpoint of the sweep are chosen such that intermittent Hartmann-Hahn resonances are guaranteed. This technique, the integrated solid effect, allows polarization transfer from a large fraction of the NV electron spins to their surrounding nuclear spins.

Therefore, the resonant double quantum transition that is mediated by far-detuned single quantum transitions combines robustness with strong electron-nuclear coupling. It is this idea and its combination with the integrated solid effect that we are going to develop and analyze in detail for realistic experimental parameters and various imperfections in this section.

1. Double quantum transition

For illustration of the basic idea, let us first consider a system that is composed of an NV center and a single ^{13}C nuclear spin in a nanodiamond of random orientation. In the laboratory frame the applied magnetic field defines the z axis, the NV is placed at the origin of the coordinate system, and the ^{13}C nuclear spin, placed near the NV center, is situated at position $\vec{r}$. A microwave (MW) field of frequency ω_M is applied as off-resonant drive of the spin transitions $|-1\rangle \leftrightarrow |0\rangle$ and $|0\rangle \leftrightarrow |+1\rangle$ while approximately satisfying a double resonance condition, that is $2\omega_M \cong E_{|+\rangle} - E_{|-\rangle}$. We chose circular polarization but linear polarization would suffice. The

Hamiltonian of the whole system is then

$$H = \Omega_M(S_x \cos\omega_M t + S_y \sin\omega_M t) + [\gamma_e B + \delta(\theta)]S_z + D(\theta)S_z^2 + g[\vec{S}\vec{I} - 3(\vec{S}\cdot\vec{e}_r)(\vec{I}\cdot\vec{e}_r)] + \gamma_n B I_z, \quad (6)$$

in which $g = \frac{\mu_0}{4\pi}\frac{\gamma_e\gamma_n}{r^3}$ with $r = |\vec{r}|$ denoting the distance from the NV spin to the nuclear spin and $\vec{e}_r = \vec{r}/r$. $\vec{I}$ is the spin-$\frac{1}{2}$ vector operator of the nuclear spin with the gyromagnetic ratio γ_n and $\Omega_M = \sqrt{2}\Omega$ is the Rabi frequency of the driving field. Assuming a point-dipole interaction and neglecting the contact term we obtain

$$H_e \simeq \Omega_M(S_x \cos\omega_M t + S_y \sin\omega_M t) + [\gamma_e B + \delta(\theta)]S_z + D(\theta)S_z^2 + \gamma_n B I_z - g S_z\{3e_r^z(e_r^x I_x + e_r^y I_y) + [3(e_r^z)^2 - 1]I_z\}. \quad (7)$$

In the interaction picture with respect to $H_0 = \omega_M S_z$, the Hamiltonian is given by

$$H' = \Omega(|-1\rangle\langle 0| + |0\rangle\langle +1| + \text{H.c.}) + \gamma_n B I_z + D(\theta)S_z^2 + \Delta S_z + S_z\cdot\mathbf{A}\cdot\vec{I}, \quad (8)$$

in which $\mathbf{A} = g\sqrt{1+3(e_r^z)^2}\vec{h} = A\vec{h}$ is the hyperfine interaction tensor for the nuclear spin, with $\vec{h}$ determined by e_r: $h_x = 3e_r^x e_r^z/\sqrt{1+3(e_r^z)^2}$, $h_y = 3e_r^y e_r^z/\sqrt{1+3(e_r^z)^2}$, and $h_z = [3(e_r^z)^2 - 1]/\sqrt{1+3(e_r^z)^2}$. The detuning Δ is given by

$$\Delta = \gamma_e B + \delta(\theta) - \omega_M, \quad (9)$$

which is a function of the NV orientation due to the second-order energy correction $\delta(\theta)$.

Since the nuclear coordinate system is arbitrary, we can redefine it by following the method in Ref. [24]. The z axis is chosen to coincide with the external magnetic field, and we define the y axis to be perpendicular to both magnetic field direction and $\vec{h}$. In the new nuclear coordinate system, the Hamiltonian is given by

$$H'' = \Omega(|-1\rangle\langle 0| + |0\rangle\langle +1| + \text{H.c.}) + D(\theta)S_z^2 + \Delta S_z + \gamma_n B I_{z'} + S_z(a_{x'}I_{x'} + a_{z'}I_{z'}) \quad (10)$$

where $I_z = I_{z'}$ and $a_{z'}$ and $a_{x'}$ are the elements of the secular and pseudosecular hyperfine interactions, respectively.

In what follows we assume that (i) $|D(\theta)| \gg \Delta$ which implies that the microwave driving field tends to be far detuned from the single quantum transitions $|-1\rangle \leftrightarrow |0\rangle$ and $|0\rangle \leftrightarrow |+1\rangle$, and (ii) $|D(\theta)| \gg \Omega$ such that the Rabi frequency is significantly smaller than the detuning [see Fig. 1(b)]. This will allow us to remove level $|0\rangle$ adiabatically from the dynamics to achieve a simplified effective Hamiltonian, Eq. (16).

To this end, we consider the dominant parts of Eq. (10) by neglecting the nuclear spins as well as ΔS_z. In the basis $\{|+1\rangle, |0\rangle, |-1\rangle\}$ we therefore consider

$$H_{NV} = \begin{pmatrix} D(\theta) & \Omega & 0 \\ \Omega & 0 & \Omega \\ 0 & \Omega & D(\theta) \end{pmatrix}. \quad (11)$$

The eigenstates and eigenenergies of H_{NV} are

$$|\mu_\mp\rangle = \frac{1}{\sqrt{2+X_\pm^2}}(|+1\rangle + |-1\rangle - X_\pm|0\rangle), \quad (12)$$

$$\omega_{\mu_\pm} = \frac{1}{2}[D(\theta) \pm \sqrt{8\Omega^2 + D^2(\theta)}] \quad (13)$$

and

$$|\lambda\rangle = \frac{1}{\sqrt{2}}(|+1\rangle - |-1\rangle), \quad (14)$$

$$\omega_\lambda = D(\theta) \quad (15)$$

with

$$X_\pm(D(\theta),\Omega) = \frac{D(\theta) \pm \sqrt{8\Omega^2 + D^2(\theta)}}{2\Omega}.$$

For $|D(\theta)| \gg \Omega$ we have two cases: $D(\theta) > 0$ leads to $X_-(D(\theta),\Omega) \sim 0$ and $X_+(D(\theta),\Omega) \gg 1$, while $D(\theta) < 0$ results in $X_+(D(\theta),\Omega) \sim 0$ and $X_-(D(\theta),\Omega) \gg 1$.

In both cases, two of the eigenstates are approximately given by $|\pm\rangle = \frac{1}{\sqrt{2}}(|-1\rangle \pm |+1\rangle)$ and form an effective two-level system while the state $|0\rangle$ does not participate in the dynamics because for $|D(\theta)| \gg \Omega$ it is far detuned. We will now focus attention on these two states $|\pm\rangle$ and write the Hamiltonian Eq. (10) in the subspace spanned by $\{|+\rangle, |-\rangle\}$ to find

$$H_\pm \simeq \pm\Omega_{\text{eff}}\sigma_z + 2\Delta\sigma_x + \gamma_n B I_{z'} + 2\sigma_x(a_{x'}I_{x'} + a_{z'}I_{z'}) \quad (16)$$

in which H_+ and H_- correspond to the cases $D(\theta) > 0$ and $D(\theta) < 0$, respectively. Here

$$\Omega_{\text{eff}} = \tfrac{1}{2}[-|D(\theta)| + \sqrt{8\Omega^2 + D^2(\theta)}]$$

and $\sigma_z = \frac{1}{2}(|+\rangle\langle +| - |-\rangle\langle -|)$, $\sigma_x = \frac{1}{2}(|+\rangle\langle -| + |-\rangle\langle +|)$, $I_{z'} = \frac{1}{2}(|\uparrow\rangle\langle\uparrow| - |\downarrow\rangle\langle\downarrow|)$, and $I_{x'} = \frac{1}{2}(|\uparrow\rangle\langle\downarrow| + |\downarrow\rangle\langle\uparrow|)$. Furthermore $|\downarrow\rangle$ and $|\downarrow\rangle$ denote the ground and excited states of the nuclear spin.

For the final step, we now restrict attention to the case where $\theta \in [0^\circ, 20^\circ]$ in which case $D(\theta) > 0$ and we consider Hamiltonian H_+. In matrix notation, the electronic part of the Hamiltonian Eq. (16) then takes the form

$$H_\Delta = \begin{pmatrix} \frac{\Omega_{\text{eff}}}{2} & \Delta \\ \Delta & -\frac{\Omega_{\text{eff}}}{2} \end{pmatrix}. \quad (17)$$

The eigenstates and eigenenergies are

$$|\chi_-\rangle = \cos\frac{\zeta}{2}|-\rangle - \sin\frac{\zeta}{2}|+\rangle,$$
$$|\chi_+\rangle = \cos\frac{\zeta}{2}|+\rangle + \sin\frac{\zeta}{2}|-\rangle, \quad (18)$$
$$\omega_{\text{eff}} = \pm\sqrt{\Delta^2 + \frac{\Omega_{\text{eff}}^2}{4}},$$

in which $\arctan\zeta = \frac{-\Delta}{\Omega_{\text{eff}}/2}$, Δ and Ω_{eff} are dependent on the angle θ between NV orientations and applied magnetic field. Defining Pauli operators $\sigma_{\tilde{x}}, \sigma_{\tilde{y}}, \sigma_{\tilde{z}}$ in the eigenbasis of H_Δ we

find

$$H_+ = 2\omega_{\rm eff}\sigma_{\tilde z} + \gamma_n B I_{z'} + 2(\sigma_{\tilde x}\sin\varphi + \sigma_{\tilde z}\cos\varphi)(a_{x'}I_{x'} + a_{z'}I_{z'}), \quad (19)$$

in which the angle φ is determined by

$$\sin\varphi = \frac{\Omega_{\rm eff}}{\sqrt{4\Delta^2 + \Omega_{\rm eff}^2}}.$$

The Hamiltonian H_+ can be simplified further under two main assumptions, namely (i) $a_{x'} \ll \gamma_n B$, that is, for weakly coupled nuclear spins, and (ii) $|\frac{\gamma_n B}{2} - \omega_{\rm eff}| \ll a_{x'}$ that is, we satisfy a Hartmann-Hahn condition. Then the polarization transfer dynamics is described by

$$H_{\rm trans} = 2\omega_{\rm eff}\sigma_{\tilde z} + \gamma_n B I_{z'} + 2a_{z'}\cos\varphi\sigma_{\tilde z}I_{z'} + \frac{a_{x'}\sin\varphi}{2}(|\chi_+,\downarrow\rangle\langle\chi_-,\uparrow| + \text{H.c.}), \quad (20)$$

where $2a_{z'}\cos\varphi\sigma_{\tilde z}I_{z'}$ does not affect the flip-flop interaction.

Let us briefly highlight the key difference of this off-resonant driving in comparison to previously introduced polarization schemes, namely its relatively high robustness with respect to the angle θ between the external magnetic field and the natural quantization axis of the NV center. If we were to follow the scheme of Ref. [24], even for $\theta = 1^\circ$, the detuning of the MW frequency from the NV electronic resonance exceeds $(2\pi)1$ MHz, which prevents efficient polarization transfer [for $\theta = 20^\circ$ we find $(2\pi)500$ MHz detuning]. In our scheme, for as long as $D(\theta) \gg \Omega$, the energy difference between the states $|-\rangle$ and $|+\rangle$ scales as $2\Omega^2/D(\theta)$ and so does the effective Rabi frequency $\Omega_{\rm eff}$. For deviation $\theta \in [0^\circ, 20^\circ]$, if $\Omega = (2\pi)65$ MHz, the effective Rabi frequency is roughly within $[(2\pi)3$ MHz, $(2\pi)3.6$ MHz], which narrows the range of the detuning of the resonant frequency.

2. Integrated solid effect

In the discussion so far, we have assumed that the electron spin of the NV center is held continuously at a Hartmann-Hahn resonance with a specific target nuclear spin to achieve polarization transfer. In practice, however, this will only capture a small fraction of the NV centers and nuclear spins as the resonance condition will depend on $\Delta = \gamma_e B + \delta(\theta) - \omega_M$ which in turn is a function of the angle θ via $\delta(\theta)$ [Fig. 2(b)]. In the range $\theta \in [0^\circ, 20^\circ]$, we have $\delta(\theta) \in [0, (2\pi)45$ MHz], as shown in Fig. 2(b) which can lead to a violation of the Hartmann-Hahn resonance for a large fraction of the NV centers. In order to achieve polarization transfer for a larger fraction of the NV centers, we will use our ability to control the strength of the externally applied magnetic field or the frequency of the applied microwave field to implement a sweep of Δ.

In order for us to understand qualitatively the conditions that such a sweep has to satisfy, we briefly examine the energy-level diagram of a system consisting of one electron and one nuclear spin as described by Eq. (20). This reveals that there are two resonance points A_1 and A_2 for $\Delta = \pm\Delta_{HH}$ owing to the symmetry of the Hamiltonian. In a fully adiabatic sweep, polarization would exchange twice and result in a vanishing net polarization transfer. Hence the sweep rate needs to be chosen such that around the A_i the system becomes nonadiabatic for the two branches including $|\chi_+,\downarrow\rangle$ and $|\chi_-,\uparrow\rangle$ as this will lead to an approximately 50% probability for polarization transfer. At the same time the sweep has to remain adiabatic with respect to the energy gap for transitions between the $\{|\chi_+,\downarrow\rangle, |\chi_-,\uparrow\rangle\}$ and the $\{|\chi_+,\uparrow\rangle, |\chi_-,\downarrow\rangle\}$ manifold as transitions between these two manifolds, induced by nonadiabaticity or in fact dephasing events, would lead to depolarization. These requirements set some limitations on the sweep rate that are, fortunately, not too stringent.

The quasiadiabatic sweep described above realizes an instance of the so-called integrated solid effect (ISE) [34] and can achieve polarization transfer between a large fraction of the NV spins and nuclear spins. Therefore, magnetic control of the nuclear spin and efficient polarization exchange become possible even for relatively large angles between the natural quantization axis of the NV center and the external magnetic field. In the following we will examine this idea in more detail.

Let us now examine two regimes of the quasiadiabatic transfer described above, namely (i) those parts of the sweep parameters that are far from the Hartmann-Hahn resonance points A_1 and A_2 which will lead to an upper bound on the sweep rate, and (ii) the behavior around the Hartmann-Hahn resonances which will provide lower bounds on the sweep rate.

For regime (i), as the coupling between electron and nuclear spin is negligible, it suffices to examine the electronic part of Eq. (16), that is

$$H'_\Delta = \begin{pmatrix} \frac{\Omega_{\rm eff}}{2} & \Delta(t) \\ \Delta(t) & -\frac{\Omega_{\rm eff}}{2} \end{pmatrix}, \quad (21)$$

in which $\Delta(t) = \gamma_e B - \delta(\theta) - \omega_M$. For simplicity we assume the detuning to vary at a constant rate $v > 0$, i.e., $\Delta(t) = \Delta(t_i) + vt$, where $\Delta(t_i)$ is the initial detuning at the start of sweep. According to the quantum adiabatic condition we require, at all times, that

$$\frac{\langle E_{1m}(t)|\dot E_{1n}(t)\rangle}{|E_{1m}(t) - E_{1n}(t)|} \gg 1, \quad m \neq n, \quad (22)$$

where $E_{1m}(t)$ and $E_{1n}(t)$ are the instantaneous eigenvalues, $|E_{1m}(t)\rangle$ and $|E_{1m}(t)\rangle$ are the eigenstates of effective Hamiltonian H_Δ, respectively. Then the condition for the sweep to be adiabatic is given by

$$\frac{\Omega_{\rm eff}^2}{|v|} \gg 1. \quad (23)$$

Adiabatic evolution implies that the initial eigenstate of this Hamiltonian H_Δ will remain close to the instantaneous eigenstate at any time during the sweep. In particular, during approach to the Hartmann-Hahn resonances and indeed during the entire sweep there will be no transitions of the type $|\chi_-,\downarrow\rangle$ to $|\chi_+,\downarrow\rangle$ which, as is easily seen by examination of Fig. 4, would have a depolarizing effect in the subsequent sweep.

To gain a feeling for the upper limit on the sweep rates that this implies for typical experimental parameters suppose as in the previous section that $\Omega = (2\pi)65$ MHz so that in the range $\theta \in [0^\circ, 20^\circ]$ we find $\Omega_{\rm eff}$ in the range $[(2\pi)3$ MHz, $(2\pi)3.6$ MHz]. This in turn implies that $v < (2\pi)10\text{MHz}/\mu\text{s}$ guarantees that the adiabatic condition is satisfied. As shown in Fig. 2(b) in this range we have

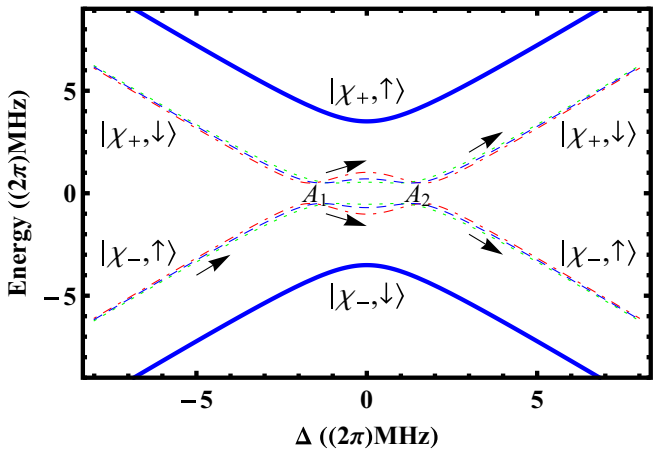

FIG. 4. (Color online) Eigenenergies of Eq. (20) for $B = 0.36$ T in which $|\frac{a_{x'}\sin\varphi_l}{2}| = (2\pi)0.5$ MHz, $\Omega_{\rm eff} = (2\pi)2.2$ MHz (dot-dashed red line), $\Omega_{\rm eff} = (2\pi)3$ MHz (dotted green line), $\Omega_{\rm eff} = (2\pi)3.6$ MHz (dashed blue line). The level diagram shows the progression of the eigenvalues of the Hamiltonian during the ISE sweep. Energies of the states $|\chi_+,\uparrow\rangle$ and $|\chi_-,\downarrow\rangle$ (solid blue line) for $\Omega_{\rm eff} = (2\pi)2.2$ MHz are included. Transitions from states represented by solid blue lines to state represented by dashed lines may lead to depolarization of the nuclear bath.

$\delta(\theta) \in [0,(2\pi)45\ \text{MHz}]$. Suppose a sweep rate $v = (2\pi)6\text{MHz}/\mu\text{s}$, then no more than 10 μs are required to cover all NV centers within $\theta \in [0^\circ,20^\circ]$. Experimentally such sweep rates are easily obtained using arbitrary wave form generators.

Let us now proceed to discuss case (ii), namely the sweep around the Hartmann-Hahn resonances which will provide lower bounds in the sweep rate. Near the resonant points, the effective Hamiltonian Eq. (20) in the subspace spanned by $\{|\chi_+,\downarrow\rangle,|\chi_-,\uparrow\rangle\}$ is well approximated by the matrix form

$$H^l_{\rm mat} = \begin{pmatrix} (-1)^l v(t-t_l)\cos\varphi_l & \frac{a_{x'}\sin\varphi_l}{2} \\ \frac{a_{x'}\sin\varphi_l}{2} & (-1)^{l+1} v(t-t_l)\cos\varphi_l \end{pmatrix}. \tag{24}$$

Here $l = 1,2$ corresponds to points A_1 and A_2, and near these two points we make use of the expansion

$$\omega_{\rm eff}(t) = \omega_{\rm eff}(t_l) + \frac{\partial\omega_{\rm eff}(t)}{\partial t}|_{t_l}(t-t_l) = (-1)^l v(t-t_l)\cos\varphi_l.$$

According to Landau-Zener (LZ) theory [35], transitions are possible between two approaching levels as a control parameter is swept across the point of minimum energy splitting. The asymptotic probability of a LZ-tunneling transition is given by

$$P_{LZ} = e^{-2\pi\mu} \tag{25}$$

where, by virtue of the Hartmann-Hahn condition $\gamma_n B = \sqrt{4\Delta^2 + \Omega^2_{\rm eff}}$ at resonant points A_1 and A_2, we find

$$\mu = \frac{\left(\frac{a_{x'}\sin\varphi_l}{2}\right)^2}{2|v|\cos\varphi_l} = \frac{\Omega^2_{\rm eff}a^2_{x'}}{8|v|(\gamma_n B)\sqrt{(\gamma_n B)^2 - \Omega^2_{\rm eff}}}.$$

This enters the unitary transformation

$$N^l = \begin{pmatrix} \sqrt{1-P_{LZ}}e^{i\tilde{\varphi}_s} & -\sqrt{P_{LZ}} \\ \sqrt{P_{LZ}} & \sqrt{1-P_{LZ}}e^{-i\tilde{\varphi}_s} \end{pmatrix} \tag{26}$$

that is taking place when traversing the avoided crossing. Here $\tilde{\varphi}_s = \varphi_s - \pi/2$ is due to the Stokes phase φ_s.

The full sweep takes the system from $\Delta \ll 0$ to $\Delta \gg 0$ across both A_1 and A_2. At each resonance point polarization transfer is possible between the electron and the nuclear spins [36]. Consider a sweep starting at $\Delta(0) \ll -\Omega_{\rm eff}$ for which the electron spin is initialized in state $|\chi_-\rangle$ and the adiabatic condition Eq. (23) is satisfied. If the nuclear spin is initially found in state $|\downarrow\rangle$, the electron-nuclear system will start and finish the sweep in state $|\chi_-,\downarrow\rangle$, i.e., the nuclear polarization is unchanged. If on the other hand the nuclear spin is initially found in state $|\uparrow\rangle$, the evolution of the system will start in $|\chi_-,\uparrow\rangle$. In this case the probability for experiencing a polarization transfer at the end of the full sweep, that is, finding the system in state $|\chi_+,\downarrow\rangle$, is given by

$$\begin{aligned} P &= P_{\rm max}\sin^2[\Phi_{St}] \\ &= 4P_{LZ}(1-P_{LZ})\sin^2[\Phi_{St}]. \end{aligned} \tag{27}$$

Here Φ_{St} is determined by the initial phase of the system and the phases acquired during the adiabatic evolution and the nonadiabatic transitions. We do not discuss these dynamical phase shifts in detail as they depend on details of the evolution and orientations that vary from NV center to NV center and it is therefore reasonable to assume that Φ_{St} is random [37,38]. Hence, when averaged over many sweeps, the average polarization transfer probability is given by

$$\overline{P} = 2P_{LZ}(1-P_{LZ}),$$

as shown in Fig. 5. The value of P_{LZ} and hence the maximum $\overline{P} = 2P_{LZ}(1-P_{LZ})$ is determined by the hyperfine coupling strength $a_{x'}$, the rate of the ISE sweep v, and to a lesser extent on the strength of the applied microwave field.

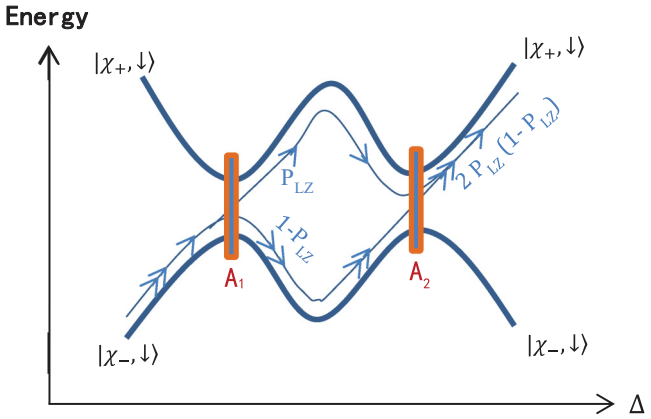

FIG. 5. (Color online) Double-passage transition. A schematics of a pair of the adiabatic energy levels as in Fig. 4. At each crossing there is a probability of P_{LZ} for a Landau-Zener transitions. The lines with one (two) arrows show the two paths where the transition to the upper level happens during passage of the first (second) resonance point. The average probability for a polarization transfer at the end of the completed passage is given by $2P_{LZ}(1-P_{LZ})$.

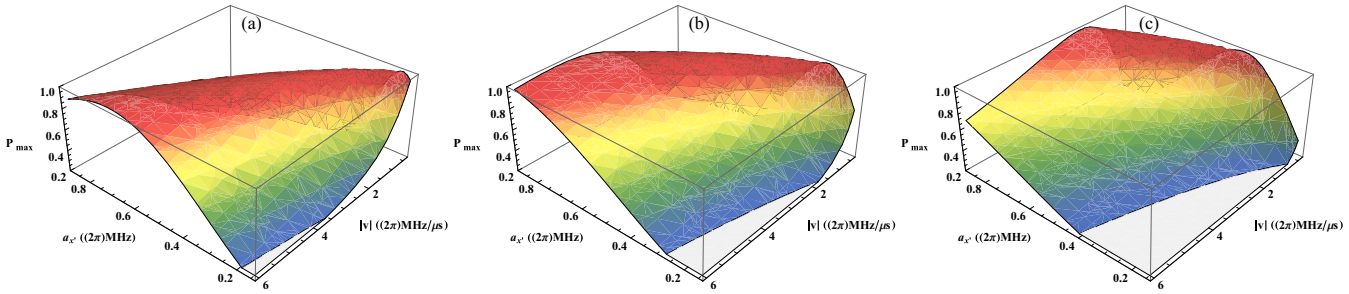

FIG. 6. (Color online) The maximal polarization transfer $P_{\max}$ as a function of the effective coupling Ω_{eff}. (a) $\Omega_{\text{eff}} = (2\pi)3.6$ MHz (b) $\Omega_{\text{eff}} = (2\pi)3$ MHz; (c) $\Omega_{\text{eff}} = (2\pi)2.3$ MHz.

It is straightforward to see that $P_{\max}$ and hence $\overline{P}$ vanish for both $v \gg 0$ and $v \to 0$, corresponding to the diabatic and adiabatic sweep. The maximum value is achieved for $P_{LZ} = 1/2$ and the parameters for achieving this maximum are quite flexible; see Fig. 6. $P_{\max}$ remains high across a wide range of sweep rates as shown in Figs. 6(a) and 6(b). Note furthermore, that for a given sweep rate we obtain efficient polarization transfer to the nuclear spins in a broad range of different microwave Rabi frequencies; see Fig. 6. For example, for $\Omega_{\text{eff}} = (2\pi)3.6$ MHz, a speed $v = (2\pi)6\text{MHz}/\mu\text{s}$ can obtain $P_{\max} > 0.2$ in the coupling range $a_{x'} \in [(2\pi)0.18, (2\pi)0.9]$ MHz. Furthermore, a slower sweep gives a better polarization transfer for a smaller effective Rabi frequency and a weaker coupling strength between the electron spin and the nuclear spin. In order to polarize the nuclear spins with larger distance from the NV spin, one can slow down the ISE sweep, or increase the Rabi frequency of the microwave field, as shown in Fig. 6(c).

C. Preparation of the initial state

So far we have assumed the preparation of a specific initial state in the polarization sequence to be achieved with perfect fidelity. However, due to the random orientations of the NV centers, optical pumping leads to the initialization of the electron spin of the NV center in a wide range of different states. Furthermore, due to the broad distribution of zero-field splittings of the NV center in randomly oriented nanodiamonds, any applied microwave field will experience an uncertain and potentially large detuning from the electronic resonance. This presents challenges to the preparation of the electron spin of the NV center in the initial state that is required for our polarization scheme. We address these challenges with an adiabatic sweep of the frequency of the microwave field which we will show to deliver robust and rapid state preparation.

Let us consider as an example the initialization of the NV center in the state $|-1\rangle$. For moderate θ optical pumping will lead to a state that possesses a significant overlap with $|0\rangle$. In order to map this state to the target $|-1\rangle$, we make use of the fact that in the relatively high magnetic fields that we are considering (e.g., $B \cong 0.36$ T) the energy gap on the $|-1\rangle \leftrightarrow |0\rangle$ transition is very different from the energy gap of the $|0\rangle \leftrightarrow |+1\rangle$ transition. Hence it is possible to use a circular polarized microwave driving field

$$H_{dr} = \Omega_{M-}(S_x \cos\omega_- t + S_y \sin\omega_- t), \tag{28}$$

in which $\Omega_{M-} = \sqrt{2}\Omega_-$ is the Rabi frequencies of the MW field, with frequency ω_- to drive dominantly the $|-1\rangle \leftrightarrow |0\rangle$ transition. The resulting effective two-level system consisting of the states $|0\rangle$ and $|-1\rangle$ can be described in the matrix representation by

$$H_{0,-1} = \begin{pmatrix} \Delta_{MW}(t)/2 & \Omega_- \\ \Omega_- & -\Delta_{MW}(t)/2 \end{pmatrix}, \tag{29}$$

in which $\Delta_{MW}(t) = \gamma_e B + \delta(\theta) + D(\theta) - \omega_-(t)$. Now we assume that $\omega_-(t)$ experiences a constant rate sweep such that $\Delta_{MW}(t) = \Delta_{MW}(t_i) + \dot{\Delta}_-(t - t_i)$. We set $t_i = 0$ for simplicity. The condition for the sweep to be adiabatic is then

$$\frac{8\Omega_-^2}{|\dot{\Delta}_-|} \gg 1. \tag{30}$$

Adiabatic evolution implies that the initial eigenstate of this Hamiltonian $H_{0,-1}$ will remain close to the instantaneous eigenstate at any time during the sweep. The eigenstates and eigenenergies are

$$|E^{\pm}(t)\rangle = \zeta_1^{\mp}(t)|-1\rangle \pm \zeta_1^{\pm}(t)|0\rangle,$$
$$E^{\pm}(t) = \pm\sqrt{[\Delta_{MW}(t)/2]^2 + \Omega_-^2}, \tag{31}$$

with $\zeta_1^{\pm} = \sqrt{\frac{E^+(t) \mp \Delta_{WM}(t)}{2E^+(t)}}$. If at the start of the sweep $\Delta_{WM}(0) < 0$ and $|\Delta_{WM}(0)| \gg 2\Omega_-$ and the electron spin is prepared in the state $|0\rangle$, the state will evolve along the path $|E^+(t)\rangle$ to end in the state $|-1\rangle$.

As an example, consider a Rabi frequency $\Omega_- = (2\pi)20$ MHz and $\theta \in [0^\circ, 20^\circ]$. Then a sweep from $\Delta_{WM}(t_i) > (2\pi)160$ MHz to $\Delta_{WM}(t_f) < -(2\pi)160$ MHz includes all NV centers in the sweep. For $|\omega_1(t_f) - \omega_1(t_i)| = \dot{\omega}_1 t_f \simeq (2\pi)870$ MHz we require $t_f \gg [\omega_1(t_f) - \omega_1(t_i)]/8\Omega_-^2 = 0.04$ μs to achieve adiabaticity. Hence very high fidelity preparation of the state $|-1\rangle$ can be achieved within 0.4 μs which is faster than the optical polarization cycle.

So far we have assumed that the optical initial state $|0\rangle$ is well prepared. However, for the relatively high magnetic fields that we are considering, the optical initial state is given by $|0\rangle_\theta = \cos\theta|0\rangle + \frac{\sin\theta}{\sqrt{2}}(e^{i\phi}|+1\rangle - e^{-i\phi}|-1\rangle)]$ [see Eq. (5)]. For a perfect adiabatic sweep we obtain the average polarization in the range $\theta \in [0^\circ, 20^\circ]$ as

$$\overline{P_{N_1}} = \frac{\int_S \left(\cos^2\theta - \frac{\sin^2\theta}{2}\right) dS}{S}. \tag{32}$$

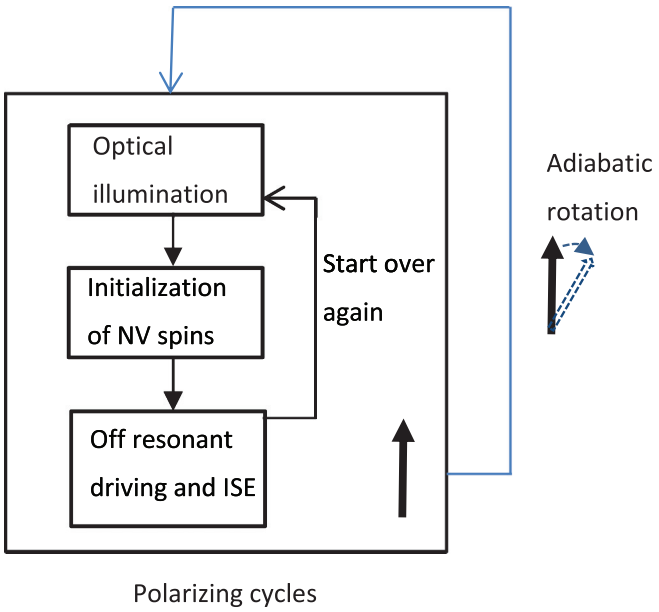

FIG. 7. (Color online) A simple flow diagram of the entire polarization scheme: For a given direction of magnetic field, the large box includes numerous polarization cycles (each polarization cycle includes optical initialization of the NV spin, adiabatic preparation of the state $|-1\rangle$, and then polarization transfer by matching a H-H resonance condition by using off-resonant microwave driving and the ISE technique). After the adiabatic rotation of the magnetic field (the thick black arrow represent the magnetic field orientation which is rotated to another direction denoted by the dashed blue arrow) we repeat our polarizing cycles to achieve the polarization of additional nuclear spins.

Here S is the surface area of the two sectors within θ deviation and dS is the corresponding area element. The reachable polarization for nearby nuclear spins and the average polarizations are $\overline{P_{N_1}} = 0.91$ for $\theta \in [0^\circ, 20^\circ]$.

D. Polarizing cycles and effective ranges

We can now summarize the polarizing cycles as follows (see also the black box of the flow diagram Fig. 7): (i) Optical pumping initializes the NV spin and (ii) a subsequent adiabatic transfer brings the electron spin to the $|-1\rangle$ state. (iii) By using off-resonant driving and a quasiadiabatic sweep across two Hartmann-Hahn resonance points (ISE technique) polarization is transferred from the NV spin to the nuclear spin. Steps (i)–(iii) are repeated as required. This method has two primary advantages: (1) the impact of the random orientations is minimized, and NV spins in a wide range of orientations are still accessible for polarization. (2) Using this method, the coupling strength between the NV and nuclear spins is doubled because it involves the double quantum transitions between the states $|-1\rangle$ and $|+1\rangle$.

In Fig. 8 we simulate many cycles of this polarization protocol for a system of one NV center and a single nuclear spin under the assumption that the NV center is initialized to the state $|-1\rangle$ as an example. The initial density matrix of the unpolarized nuclear spin is $\rho_0 = \mathbf{I}/2$, with $\mathbf{I}$ being the unit matrix. For the state ρ_k of the nuclear spin after the kth iteration of the polarization protocol we have the following relation:

$$\rho_{k+1} = \mathrm{tr}_e[U_t(\rho_k \otimes |\chi_-\rangle\langle\chi_-|)U_t^\dagger], \tag{33}$$

where $U_t = e^{-\int i H_{\mathrm{trans}} dt}$ is time evolution operator and H_{trans} is the Hamiltonian Eq. (20); we denote by Δt the sweep time and by tr_e the trace over the electron spin. The polarizing P is defined as $P = \langle I_{z'}\rangle/\langle I_{z'}\rangle_0$ with $\langle I_{z'}\rangle$ denoting the expectation value of the nuclear spin and $\langle I_{z'}\rangle_0$ the expectation value of the completely polarized state.

Finally, as we have discussed in the previous sections, the ISE requires an adiabatic slow passage. For $\theta \in [0^\circ, 20^\circ]$ we find $\delta(\theta) \in [0, (2\pi)45\ \mathrm{MHz}]$ and in order to include the entire range of detunings in the sweep we can estimate the required polarizing time. At a sweep rate of $v = (2\pi)6\mathrm{MHz}/\mu\mathrm{s}$ we find $\Delta t \sim 10\ \mu$s. In Fig. 8(a), assuming the perfect initialization of the NV spin in the state $|-1\rangle$, we take one nuclear spin with the typical coupling $a_{x'} = (2\pi)0.6$ MHz as an example to demonstrate the polarization transfer [the nuclear spin is about 0.5 nm from the NV spin and $a_{z'} = (2\pi)0.64$ MHz]. Here the polarization transfer after the first cycle, P_1, does not quite achieve the maximum possible value in Fig. 6 due to the existence of the phase shift Φ_{St}; more precisely $P_1 = 0.58 < P_{\max} = 0.7$ when $\Omega_{\mathrm{eff}} = (2\pi)3$ MHz [see both Figs. 6(b) and 8(a)]. Simulations for different hyperfine couplings are shown in Fig. 8(b). Again the sweep rate $v = (2\pi)6\mathrm{MHz}/\mu\mathrm{s}$ and polarization is transferred to the nuclear spins with different coupling to the NV spin, which agree with Fig. 6. Additionally, slowing

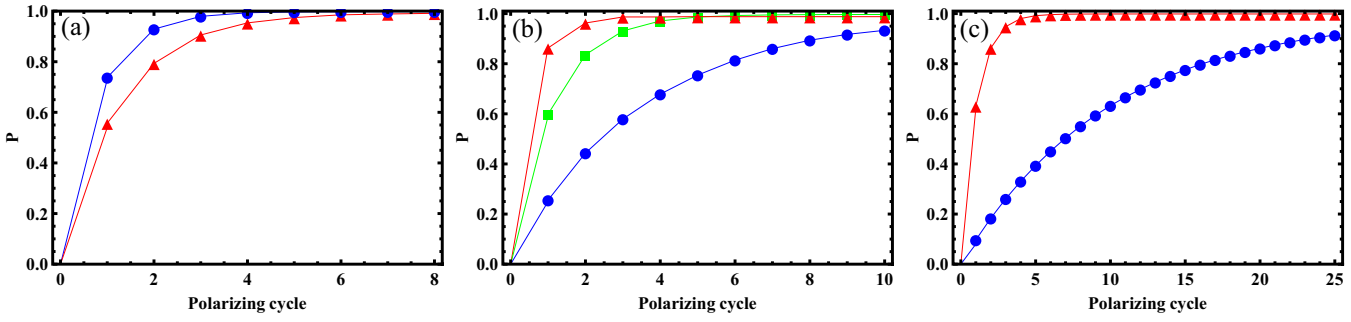

FIG. 8. (Color online) Exact polarization dynamics with $B = 0.36$ T, $v = (2\pi)6\mathrm{MHz}/\mu\mathrm{s}$ and $\Delta t = 10\ \mu$s: (a) The coupling strength is given as $a_{x'} = (2\pi)0.6$ MHz, $\Omega_{\mathrm{eff}} = (2\pi)3$ MHz (blue circles), and $\Omega_{\mathrm{eff}} = (2\pi)3.6$ MHz (red triangles). (b) We have $\Omega_{\mathrm{eff}} = (2\pi)3.5$ MHz, $a_{x'} = (2\pi)0.7$ MHz (red triangles), $a_{x'} = (2\pi)0.5$ MHz (green cubes), and $a_{x'} = (2\pi)0.3$ MHz (blue circles). (c) Exact polarization dynamics with $v = (2\pi)0.8\mathrm{MHz}/\mu\mathrm{s}$, $\Delta t = 50\ \mu$s, and $\Omega_{\mathrm{eff}} = (2\pi)2.3$ MHz, $a_{x'} = (2\pi)0.3$ MHz (red triangles), and $a_{x'} = (2\pi)0.1$ MHz (blue circles).

down the ISE sweep, as shown in Fig. 8(c) for a sweep rate $v = (2\pi)0.8\text{MHz}/\mu\text{s}$ we can polarize more distant nuclear spins with a coupling strength $a_{x'} = (2\pi)0.1$ MHz, which corresponds to a distance of about 1 nm from the NV center. This coupling is approaching the limitation of our polarization scheme, since the rotating-frame spin-lattice relaxation time of NV spin in nanodiamonds is estimated to be about 100 μs which places a lower limit of the duration of the full sweep [39].

III. BENEFIT OF ADIABATIC ROTATIONS

The NV polarization in our scheme is limited by the adiabatic sweep range and efficiency of the initialization of NV spins, enabling the polarization up to a maximum angle between NV center and external magnetic field. As discussed above, our scheme certainly performs well for NV centers whose orientation forms an angle of less than 20° from the externally applied magnetic field (and may potentially work for somewhat larger angles). It is however desirable to extend the polarization to a larger fraction of the nanodiamond ensemble, ideally covering the entire solid angle. One method for achieving this applies an adiabatic change of the orientation of the magnetic field relative to the NV center, either by rotation of the magnetic field or by rotation of the nanodiamond. For example, following the magnetic field rotation to the Z' direction, another set of NV centers with orientations in a solid angle (shown in red in Fig. 9) around the new magnetic field direction will participate in the polarization dynamics while the NV centers in the original orientations (the blue cone in Fig. 9) will be inactive. Hence previously polarized nuclear spins will not be affected by the polarization sequences, but these nuclear spins may use this "idle" time to spread their polarization by spin diffusion across larger volumes until further rotations subject them to another polarization cycle.

More specifically, let us consider the rotation of the magnetic field as an example. The Hamiltonian that is describing the rotation of the magnetic field from the Z direction to the Z' direction is given by

$$H_B = \gamma_N B_Z[\cos(\dot{\vartheta}t)I_Z + \sin(\dot{\vartheta}t)I_X] = \gamma_N B_Z I_{\vartheta(t)},$$

where $\vartheta(t) = \dot{\vartheta}t$ is the angle between the rotated magnetic field and its initial direction and $\gamma_N B_Z = (2\pi)4$ MHz.

Similar to the discussion in the initialization scheme, the well-known adiabatic condition requires $\dot{\vartheta} \ll 2\gamma_N B_Z$. For a rotation by $\vartheta = 180°$ this leads to the condition $t_r \gg 0.078\ \mu$s for the minimal rotation time t_r. This implies that $t_r \cong 0.78\ \mu$s will ensure adiabaticity and minimal perturbation of nuclear spin polarization for a rotation to an arbitrary orientation. This rotation time is much shorter than even a single polarization cycle. Hence, after running a few polarization cycles that achieve a high net polarization of nuclear spins for NV centers oriented along the Z direction, we can adiabatically rotate the magnetic field to another direction. The polarization of the nuclear spins will then be achieved for this new direction, as shown in Fig. 9. Note though that the rapid rotation of a strong magnetic field is challenging. Hence one needs to resort either to a mechanical rotation of the sample as a whole or, as explained in the next section, make use of the Brownian rotation of nanodiamonds in solution.

In addition to the rotation of the externally applied magnetic field for nanodiamond powder, another option consists of the use of random Brownian rotations of nanodiamonds in a solution. If the Brownian rotation is sufficiently slow to satisfy our adiabatic rotation condition, the polarized nuclear spins will maintain their polarization in the direction of the externally applied magnetic field. The time scale of Brownian rotations is determined by [40]

$$\tau_B = \frac{3V_H\eta}{kT}, \tag{34}$$

where k is the Boltzmann constant, T is the temperature, V_H is the hydrodynamic volume of the particle, and η the viscosity of the surrounding carrier liquid. Note that the hydrodynamic volume is an effective volume that includes both the true particle volume and the volume of a fluid that is displaced when the particle rotates due to particle-fluid interaction. A

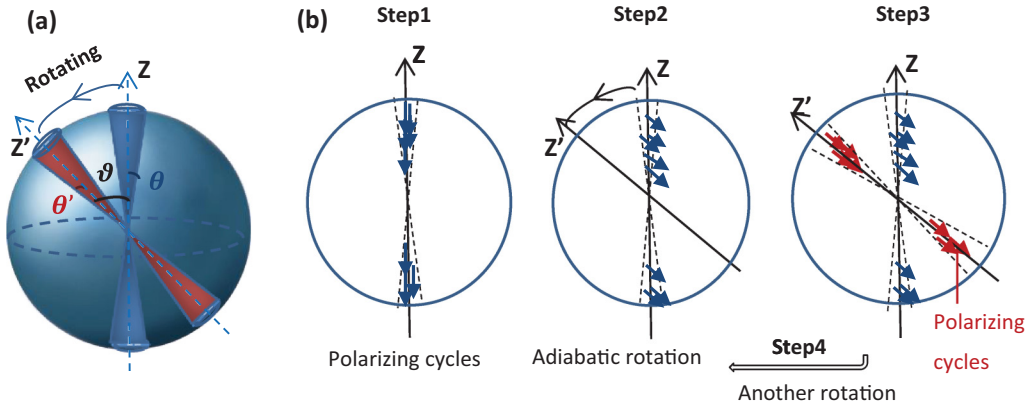

FIG. 9. (Color online) (a) Diagram of adiabatic rotating direction of the magnetic field. Blue spherical sectors present $\theta°$ deviation tolerance for Z direction of the magnetic field. Magnetic field is rotated by angle ϑ to get red spherical sectors with the half angle of the cone angle θ' to be involved. (b) Flow diagrams of polarizing steps of our scheme related to the adiabatic rotations of the magnetic field. The small blue and red arrows are the nuclear spins nearby the different NV spins in different spherical sectors. Four steps are given for our polarizing scheme. We use two-dimensional plotting for simplicity, the sphere is presented by a circle, and the areas formed by the dashed lines denote the corresponding spherical sectors. It is shown by the arrows that all the nuclear spins follows the rotated magnetic fields.

typical average hydrodynamic diameter for nanodiamonds of 30 nm in water gives a Brownian relaxation time of $\tau_B \simeq 9$ μs, which is comparable with our polarizing cycle time. One can increase the Brownian relaxation time by using nanodiamonds with a larger diameter, a more viscous fluid, or lower temperatures. Additionally, surface coating can increase the average hydrodynamic diameter, i.e., after adsorption of ferritin the diameter of nanodiamond was determined to be 85 nm [41].

Here we assume that the hydrodynamic diameter of nanodiamond is 85 nm, and the Brownian relaxation time is $\tau_B \simeq 205$ μs. On average after a time τ_B, the nanodiamonds will have rotated to another random direction, and different NV centers will now participate in the polarization dynamics of nearby nuclear spins while other NV centers will be inactive as they are effectively decoupled from their neighboring nuclear spin due to the absence of a Hartmann-Hahn condition. When an NV center "leaves" the coherent exchange range via a random rotation, the polarization of the polarized nuclear spins will still be transferred to the other nuclear spins by spin diffusion. Considering maximum of 20° deviation, 6% of the NV spins are involved at each given time, and each NV will be in this range after 16 random rotations on average.

IV. INTERNUCLEAR INTERACTION AND SPIN DIFFUSION

So far, we have considered polarization of an individual nuclear spin and have therefore ignored the effects of internuclear coupling on both the polarization cycle and on the nuclear-spin polarization diffusion towards more distant nuclear spins that are not directly interacting with the NV center. This section discusses these effects of nuclear dipolar interactions. Considering our off-resonant driving in the dressed state basis and the suitable rotating frame, the effective Hamiltonian of the whole system consisting of an NV spin and its nearby nuclear spins can be written as

$$H_{\rm tot} \approx H_{NV} + H_{hf} + H_{d-d} + H_{Nu}. \tag{35}$$

Here H_{NV} denotes the NV center effective energy Hamiltonian, H_{hf} is the effective electron-nuclear hyperfine interaction, H_{d-d} is the dipole-dipole coupling among nuclear spins, and H_{Nu} is the magnetic field splitting of nuclear spins,

$$H_{NV} = 2\Delta(t)\sigma_x + \Omega_{\rm eff}\sigma_z, \tag{36}$$

$$H_{hf} \simeq \sum_i \sigma_x \left(2a_{x_i'} I_i^{x'} + 2a_{z_i'} I_i^{z'}\right), \tag{37}$$

$$H_{d-d} \simeq \sum_{ij,j>i} d_{ij}[\vec{I}_i\vec{I}_j - 3(\vec{I}_i\cdot\vec{e}_{r_{ij}})(\vec{I}_j\cdot\vec{e}_{r_{ij}})], \tag{38}$$

$$H_{Nu} = \sum_i \gamma_n B I_i^{z'}, \tag{39}$$

with $a_{x_i'}$ and $a_{z_i'}$ denoting the hyperfine coupling strength between the ith nuclear spin and the electron spin. $d_{ij} = \frac{\mu_0}{4\pi}\frac{\gamma_n\gamma_n}{r_{ij}^3}$ is the coupling strength between the i and j nuclear spins. with $r_{ij} = |\vec{r}_{ij}|$ denoting the distance between the two nuclear spins and $\vec{e}_{r_{ij}} = \vec{r}_{ij}/r_{ij}$. The i and j indices are summed over all nuclei.

In order to estimate the effect of internuclear interactions on the polarization transfer from the NV center to the nuclei in the multiple nuclear-spins case we consider five nuclear spins and one electron spin, including hyperfine and nuclear dipolar couplings. After each polarization cycle, the electron spin is re-initialized in the state $|-1\rangle$. The concatenated evolution of the nuclear-spin density matrix is determined by an equation analogous to Eq. (33). The initial density matrix of the five unpolarized nuclear spins can be written as $\rho_0 = \mathbf{I}/2^5$, with $\mathbf{I}$ being a unit matrix of dimension 2^5, and the time evolution is given by the operator $U_t = e^{-i\int H_{\rm tot}dt}$, with $H_{\rm tot}$ denoting the total Hamiltonian Eq. (35). The polarization is defined as in Sec. II, $P_k = \langle I_{z'}^k\rangle/\langle I_{z'}^k\rangle_0$ in which the subscript k presents different nuclear spins and $P = \frac{1}{5}\sum_k^5 P_k$. We assume in these simulations only nearest neighbor internuclear-spin coupling with rates $d_{12} = d_{23} = d_{34} = d_{45} = 2$ kHz.

The simulation results are presented in Figs. 10(a) and 10(b). We consider the case that the NV is strongly coupled to all five ^{13}C spins, $a_{x_1'} = (2\pi)0.7$ MHz, $a_{x_2'} = (2\pi)0.5$ MHz, $a_{x_3'} = (2\pi)0.4$ MHz, $a_{x_4'} = (2\pi)0.32$ MHz, and $a_{x_5'} = (2\pi)0.2$ MHz. The polarization is built up for all the five nuclear spins with different coupling to the NV spin, which matches our theory. In this case, the coupling between the nuclear spins is too small to affect the evolution of the polarization dynamical built up [Fig. 10(a)]. Due to small interaction among the nuclear spins, there is almost no difference between polarization in the presence or absence of the interactions among the nuclear spins, which means our scheme works in the frozen core.

Now we would like to exemplify the benefits of internuclear interactions which leads to nuclear-spin diffusion and a considerable extension of the range of polarization. Suppose a typical configuration of nuclear spins distributed around the NV. To estimate the polarization efficiencies in a large system, we adopted the simple spin temperature approximation, namely neglecting the nuclear-spin coherence [42], which provides a good estimation of polarization transfer efficiency when the sweep time step is sufficiently small. This approximation yields independent rate equations for each individual nuclear spin and should give a conservative estimate for the achieved polarization. For the Δt sweep times described above, this approximation serves as a lower bound, as the achieved polarization in one cycle with our scheme is higher than the polarization achieved during the same time with small sweep steps.

For the diffusion step, the interaction between the nuclear spins is taken into account, where we use the Gaussian approximation for the nuclear spins. As is typical for paramagnetic centers, the NV center strongly affects the spin diffusion in nearby nuclear spins (the "frozen core") due to the energy mismatch caused by the S_zI_z hyperfine term. However, when the NV center is in the $|m_s = 0\rangle$ state, this energy mismatch is suppressed and diffusion to external nuclear spins is allowed. To give a conservative estimate, we assume that no diffusion in the frozen core takes place when the NV center is in the $|m_s = \pm 1\rangle$ states. For this purpose, we simulate the NV center as a classical spin with the probability of being in each eigenstate given by the optical initialization corresponding to the NV orientation.

As the nanodiamonds are in a solution, we assume that the differences in polarization transfer for the different

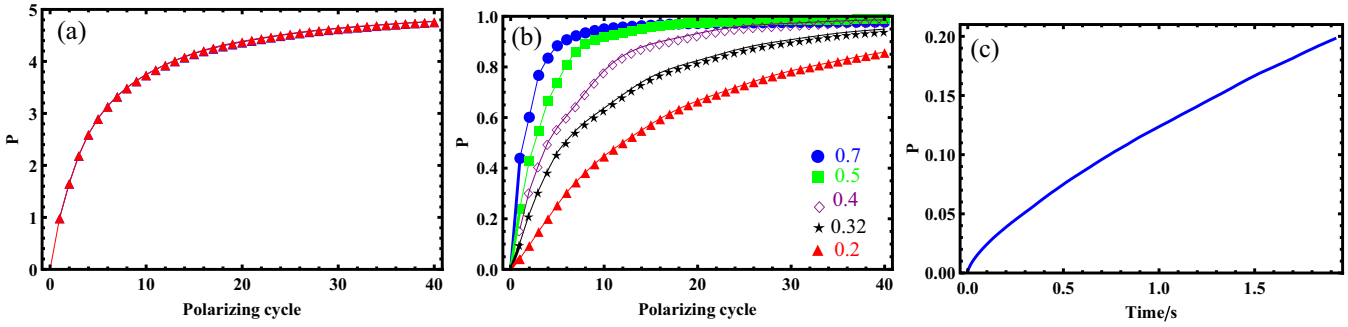

FIG. 10. (Color online) The polarization buildup for five nuclear spins for $\Omega_{\rm eff} = 3.23$ MHz. The nuclear spins are strongly interacting with the NV center spin, $a_{x'_1} = (2\pi)0.7$ MHz, $a_{x'_2} = (2\pi)0.5$ MHz, $a_{x'_3} = (2\pi)0.4$ MHz, $a_{x'_4} = 0.32$ MHz, and $a_{x'_5} = (2\pi)0.2$ MHz. (a) The blue and red triangles denote the presence and absence of the interaction among the nuclear spins. Internuclear interactions do not lead to significant changes in the polarization dynamics because the dipole-dipole interaction of nuclear spins is much smaller than the electron-nuclear coupling. (b) The polarization dynamics of the individual nuclear spins in the set of five spins represented by different markers within different colors. (c) Numerical simulation of the polarization buildup in a large number of polarization cycles in a system consisting of an NV spin and around 548 ^{13}C nuclear spins in a volume of 50 000 lattice sites by using Brownian rotation. The internuclear dynamics is treated within the bosonic approximation and we simulate a polarization buildup time of 2 sec. The system benefits from polarization diffusion between nuclear spins resulting in a high level of polarization.

orientations of the NV spins within the 20° deviation range can be neglected. Consider a random configuration of nuclear spins, with 548 nuclear spins in the vicinity of an NV center (lattice of 50 000 nuclei per NV center) whose orientation is within the 20° deviation range. The net polarization is built up by using Brownian rotations as shown in Fig. 10(c). There are two steps in the simulation. First, we assume that the orientation of the NV center satisfies $\theta \in [0°,20°]$ and we consider $\Omega_{\rm eff} = (2\pi)2.3$ MHz, sweep rate of $v = (2\pi)0.8{\rm MHz}/\mu{\rm s}$, and $\Delta t = 70\mu$s. The polarization transfer from the NV center to the neighboring nuclear spins is achieved by using our combination of off-resonantly driven double quantum transition and the ISE technique. The polarizing cycles are repeated during the Brownian relaxation time $\tau_B = 205$ μs. Second, after the Brownian relaxation time, the nanodiamond is randomly rotated to another direction. As we discussed in Sec. III, it takes roughly 3.5 ms for the nanodiamond to rotate back to our maximal deviation range for polarization, and nuclear-spin diffusion dominates during this time period (taking into account the NV effect on diffusion in the frozen core). In this step more distant nuclear spins can become polarized by diffusion. These two steps occur sequentially over a 2-sec time range. In line with previous sections, the polarization is defined as $= \langle I_{z'}\rangle/\langle I_{z'}\rangle_0$, where $I_{z'} = \sum_i^M I_i^{z'}$, M is the number of the involved nuclear spins. Interestingly, the slope of polarization is close to linear. This demonstrates that in the long diffusion time, where the nanodiamond is not involved in the polarization cycles, we do not see a bottleneck caused by slow diffusion and significant polarization is transferred from the NV spin to the nuclear spins within each step 1. The final net polarization reaches 0.2, equivalent to about 110 ^{13}C fully polarized spins are polarized within 2 sec in our scheme.

V. A LARGE ANGLE POLARIZATION SCHEME

So far we have concentrated so far on a range of angles $\theta \in [0°,20°]$ between the NV center and the external magnetic field. Note however, that this is not the only range in which efficient polarization transfer can be achieved. Indeed, we have another interesting range of the NV orientations, concentrated around the direction perpendicular to the magnetic field, i.e., $\theta \in [70°,110°]$, which involves 34% of the NV spins. Here the condition $D(\theta) < 0$ leads to the Hamiltonian H_- in Eq. (16). Following steps that are analogous to those leading up to Hamiltonian Eq. (20) we find for the subspace $\{|\chi_-,\downarrow\rangle,|\chi_+,\uparrow\rangle\}$

$$H_{\rm matrix} = \begin{pmatrix} \omega_{\rm eff} - \frac{\gamma_n B}{2} & \frac{a_{x'}\sin\varphi}{2} \\ \frac{a_{x'}\sin\varphi}{2} & -\omega_{\rm eff} + \frac{\gamma_n B}{2} \end{pmatrix}. \qquad (40)$$

Suppose now that the NV center is initialized in state $|-1\rangle$ by using the off-resonant driving. Then we make use of the ISE technique to sweep adiabatically across the two possible Hartmann-Hahn resonance points of the dressed NV spin and nuclear-spin pair. As a result the population is transferred between $|\chi_-,\downarrow\rangle$ and $|\chi_+,\uparrow\rangle$, with the other states being unaffected. As before, this allows the nuclear spins to be polarized but now in a direction opposite to the case $\theta \in [0°,20°]$. In the following we discuss the details of this case.

A. Initial polarization of the NV spins

We begin with a discussion of the initialization of the NV center spins. As explained in previous sections, optical pumping of the NV spins results in the $|m_s = 0\rangle$ state in the NV frame, that is

$$|0\rangle_\theta = \cos\theta|0\rangle + \frac{\sin\theta}{\sqrt{2}}(e^{i\phi}|+1\rangle - e^{-i\phi}|-1\rangle),$$

where the states $|0\rangle,|\pm 1\rangle$ are defined in the laboratory frame. For $\theta \in [70°,110°]$ the population in state $|0\rangle$ is very small and the initial state is well approximated by $\frac{1}{\sqrt{2}}(e^{i\phi}|+1\rangle - e^{-i\phi}|-1\rangle)$ which, in the relevant subspace spanned by $\{|+1\rangle,|-1\rangle\}$, is unpolarized.

We address this problem by means of an adiabatic sweep. For concreteness, consider $\Omega = (2\pi)20$ MHz and an

adiabatic sweep from $\Delta_{WM}(t_i) = (2\pi)320$ MHz to $\Delta_{WM}(t_f) < -(2\pi)320$ MHz. For a sweep range $|\omega_1(t_f) - \omega_1(t_i)| \simeq (2\pi)640$ MHz, the time for an adiabatic sweep is of the order of 0.4 μs. Such a sweep induces an adiabatic population transfer from state $|-1\rangle$ to state $|0\rangle$ so that the state of the NV center evolves to

$$|0\rangle_\theta \longrightarrow \cos\theta|-1\rangle + \frac{\sin\theta}{\sqrt{2}}(e^{i\phi}|+1\rangle - e^{-i\phi}|0\rangle),$$

where we ignore any dynamical and geometric phase that has been accumulated in the sweep. It is now crucial to note that the state $|0\rangle$ does not contribute to the polarization dynamics as it does not take part in the far detuned dynamics that is induced by the applied microwave fields. Hence the relevant quantity is the polarization in the subspace spanned by the states $\{|+1\rangle,|-1\rangle\}$. Normalized by the population that is found in this subspace we find

$$\overline{P^r_{N_2}} = \frac{\int_S N_r\left(\frac{\sin^2\theta}{2} - \cos^2\theta\right)dS}{S}, \tag{41}$$

where $N_r = 1/(\frac{\sin^2\theta}{2} + \cos^2\theta)$ is the normalized coefficient and $\overline{P^r_{N_2}} \sim 0.85$.

B. The sweep range for ISE

Owing to the different behavior of the energy shifts $D(\theta)$ and $\delta(\theta)$ we need to change the sweep range in the ISE. In order to achieve optimum polarization transfer, we choose $\Omega = (2\pi)40.5$ MHz, which results in a range of effective Rabi frequency $\Omega_{\text{eff}} \in [(2\pi)2.3\,\text{MHz},(2\pi)3.6\,\text{MHz}]$. The adiabatic slow passage needs to cross the range $\Delta \in [-(2\pi)21\,\text{MHz},(2\pi)21\,\text{MHz}]$. For a sweep rate of $v = (2\pi)6\text{MHz}/\mu\text{s}$ we estimate the required polarizing time as $\Delta t > 7\,\mu$s. Apart from these parameter changes, the principles underlying our discussion of the polarization transfer in Sec. II are still valid.

If we assume that the NV spin is initial polarized perfectly, we have $P_{\max} > 0.2$ in a coupling range $a_{x'} \in [0.4,0.9]$ for $|\Omega_{\text{eff}}| = (2\pi)2.27$ MHz in Fig. 6(c), compared to $a_{x'} \in [0.18,0.9]$ for $|\Omega_{\text{eff}}| = (2\pi)3.6$ MHz in Fig. 6(a). We can say that our off-resonant driving and ISE technique allow polarization transfer for all the NV orientations within $\theta \in [70^\circ,110^\circ]$. Considering that the average polarization of the NV spins in this case is about 0.5 and twice the effective Rabi frequency range here, applying a single sweep speed becomes not very efficient for all the NV orientations, especially for the nuclear spins with weak couplings to the NV spin. As we discussed, we have another choice: slowing down the ISE sweep can involve the nuclear spins with weaker coupling to the NV spin, i.e., as shown in Fig. 8(c), we can use another a speed rate $v = (2\pi)0.8\text{MHz}/\mu\text{s}$ ($\Delta t \sim 50\ \mu$s) to make it possible to polarize the ^{13}C spins with coupling strength $a_{x'} = (2\pi)0.1$ MHz.

In conclusion, off-resonant driving and the ISE technique allow for polarization transfer between the NV spin and its surrounding nuclear spins, when the orientation of the NV spin matches $\theta \in [70^\circ,110^\circ]$, but we need to sacrifice half the population to provide a high initial polarization of the dressed NV spins. On the other hand the fact that around 34% of the NV centers participate in the polarization dynamics even without magnetic field rotation is an attractive feature.

VI. DEPOLARIZING EFFECT

Our approach to increase the fraction of NV center that participates in the polarization sequences by means of adiabatic rotations may potentially have an undesired side effect as nuclear spins that have been polarized for one magnetic field orientation may be depolarized again when transferred to a different magnetic field orientation. Consider for example the case shown in Fig. 9 where, after polarization transfer is achieved for the blue spherical sectors, the magnetic field is rotated from the Z direction to a different direction Z'. If the NV spins in the blue sectors have not been polarized in advance and our combination of off-resonant driving and ISE achieves a Hartmann-Hahn condition at some instant, then the depolarized state of the NV center will be transferred to nuclear spins, whose polarization reduces as a result. In the protocol for the case $\theta \in [0^\circ,20^\circ]$ this depolarization is negligible due to the rapid increase of the detuning $\delta(\theta)$ outside of this range. Only NV centers in the range $\theta \in [20^\circ,25^\circ]$ may still experience undesired resonances. As these NV centers are still well initialized by means of optical pumping, depolarization is negligible.

The situation is different and indeed more complex for the second protocol that covers the range $\theta \in [70^\circ,90^\circ]$. NV centers with orientations in the range $\theta \in [35^\circ,43^\circ]$ are difficult to be polarized to the required state. Unfortunately, they have almost the same energy distributions $|D(\theta)|$ and $\delta(\theta)$ as the NV centers in the range $\theta \in [70^\circ,110^\circ]$; see Fig. 2. Our off-resonant driving and ISE technique scheme can lead to Hartmann-Hahn resonances at some instant which then cause polarization exchanges between the unpolarized NV centers and the polarized nuclear spins. Thus, magnetic field rotations could lead to depolarization dynamics in the previously polarized nuclear spins for the protocol that is adapted to the case $\theta \in [70^\circ,110^\circ]$.

We consider a simple system consisting of one NV and one nuclear spin as an example for studying the depolarizing effect of this case. The depolarizing cycle time is the same as our polarizing cycle time, since every initialization process is implemented on all the NV spins. Consider a nuclear spin that is initially polarized and in contact with an unpolarized electron spin $\rho_{e0} = \mathbf{I}/2$. The evolution of the nuclear-spin density matrix is then given by

$$\rho \to \cdots U'_t \text{tr}_e[U'_t(|\downarrow\rangle\langle\downarrow| \otimes \rho_{e0})U'^\dagger_t] \otimes \rho_{e0} U'^\dagger_t \ldots, \tag{42}$$

where $U'_t = e^{-i\int H^{\delta'}_{\text{matrix}}dt}$ is time evolution operator. $H^{\delta'}_{\text{matrix}}$ is given by Eq. (20) with the choice $\Omega_{\text{eff}} = (2\pi)3.5$ MHz and δ' denoting that a magnetic field in the Z' direction is being considered. The polarization P of the nuclear spin is defined as in Sec. II. As shown in Fig. 11, the nuclear spin is depolarized very rapidly. The depolarization range $\theta' \in [35^\circ,43^\circ]$ includes 9% of the NV orientations while the range in which the polarization is active includes 34% of the NV centers. Hence, although adiabatic rotation of the magnetic field brings an unexpected depolarizing effect, it is nevertheless quite attractive as the fraction of NV spins that are contributing

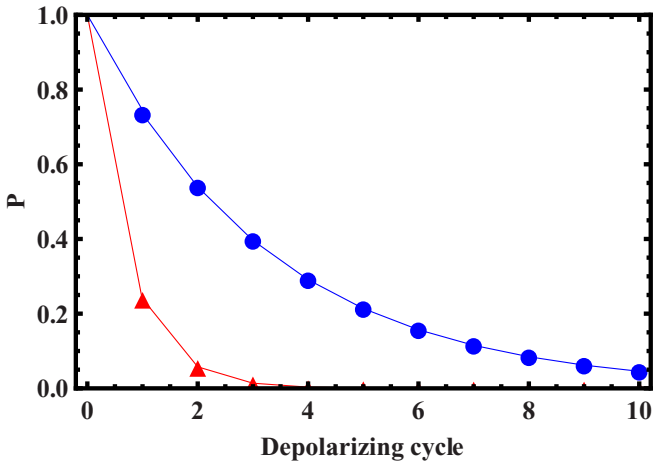

FIG. 11. (Color online) The depolarization of the previously polarized nuclear spin with $B = 0.36$ T, $\Omega_{\text{eff}} = (2\pi)3.5$ MHz, $v = (2\pi)6\text{MHz}/\mu\text{s}$, and $\Delta t = 10$ μs. The coupling strength is given as $a_{x'} = (2\pi)0.3$ MHz, (blue circles) and $a_{x'} = (2\pi)0.6$ MHz (red triangles).

to the polarization transfer even without magnetic field rotation strongly outweighs the small fraction of 9% of the NV centers that suffer depolarization.

VII. DISCUSSION

To summarize, our polarization scheme for ensembles of nanodiamonds (see Fig. 7 and Fig. 9) is as follows.

Step 1: A moderate to strong magnetic field is applied along the Z direction (of order $B = 0.36$ T). A polarization cycle consists of optically pumping and initialization of the NV center spins, and the subsequent application of off-resonant microwave driving and the integrated solid effect to realize a robust adiabatic sweep across Hartmann-Hahn resonance points. This achieves the coherent polarization transfer from the NV center spins to the nuclear spins with a range of orientations of the NV center relative to the magnetic field. This polarization cycle is repeated several times.

Step 2: Adiabatic rotations (of the magnetic field or of the nanodiamonds) change the magnetic field orientation relative to the NV centers to a new Z' direction, while the nuclear spins follow the direction of the magnetic field.

Step 3: Repeat steps 1 and 2.

Apart from control imperfections, the achievable ^{13}C-bath spin polarization will be limited by the spin-lattice relaxation time T_1 of the nuclear spins. In recent experiments, by using electron paramagnetic resonance (EPR), solid-state NMR, and DNP techniques, a variety of nanodiamond samples, of varying manufacturing processes and particle sizes, were examined [16,18,43]. Several types of nanodiamonds, especially those milled from diamonds produced from high-pressure, high-temperature (HPHT) methods exhibit very long nuclear-spin lifetimes, up to several minutes. As bulk diamonds with a comparable paramagnetic impurity concentration can exhibit nuclear-spin relaxation times of several hours, surface impurities are considered to form one of the main sources for relaxation in nanodiamonds. This is also supported by the correlation between nanodiamond size and nuclear relaxation times [16,43]. This suggest that the nanodiamond relaxation time may be improved by surface cleaning and treatment of the nanodiamonds [44,45].

Additionally, the polarization transfer rests on NV spins having a sufficiently long rotating-frame spin-lattice relaxation time $T_{1\rho}$ in nanodiamonds during the adiabatic passages that are required for the implementation of ISE. Using a strong MW field driving, $T_{1\rho}$ can be estimated as 100 μs [39,46], which is much longer than our sweep time in one polarization cycle. Assuming a polarization cycle duration of $\Delta t = 10$ μs, when rotating the magnetic field, 17 rotations of the magnetic field are required to involve all the NV spins. For a nuclear-spin lifetime of more than 2 min, this would allow the execution of around 10^5 polarization cycles for each NV spin involved before the nuclear spins start to relax. For nanodiamonds in a solution, each nanodiamond is involved in the polarization cycles roughly once every 17 random Brownian rotations. Assuming $\tau_B \simeq 205$ μs, with a pure nuclear diffusion period of roughly 3 ms after every Brownian relaxation time τ_B, 2 min lifetime of the nuclear spin would allow in excess of 10^5 polarization cycles for every NV center.

We can now obtain a rough estimate of the total amount of the net polarization that could be achieved under realistic experimental conditions. Consider a $1 - \text{mm}^3$ nanodiamond powder, dissolved in a solution. The nanodiamonds are assumed to have a diameter of 85 nm, with an NV center concentration of $C = 2 \times 10^{18}$ cm^{-3} (see [47] and references therein for achievable NV concentrations). In the limit of a uniform spatial distribution, this gives about 642 NV spins per nanodiamond, with the total amount of NV spins given by 8.35×10^{15} NV spins. Considering the natural abundance of the ^{13}C spins (1.1%), the total nuclear spins in this powder of nanodiamond is approximately 8.18×10^{18} [48]. Taking account of the high degree of nuclear polarization achieved, in excess of 0.2 as demonstrated in Sec. IV, we find that a total amount of polarization equivalent to 1.6×10^{18} nuclear spins should be achievable in such a sample within 2 sec.

The 20% nuclear-spin polarization that may be achieved with our method compares favorably with the thermal polarization of 0.1% of nonoptically excited electron spins at the moderate magnetic field of $B = 0.36$ T which sets an upper limit on the achievable nuclear-spin polarization in such protocols. Thus, even compared with the theoretical limit reachable via polarization transfer from regular electron spins to nuclear spins, the polarization reached by optical DNP and our protocols is more than 100 times larger. Cryogenic environments and higher magnetic fields dissolution-DNP methods could be used for obtaining comparable polarization, but these require much longer time for polarization (1 h) as well as expensive cryostats and hardware. Furthermore, not all diamond nanoparticles that have been functionalized with biomacromolecules may be hyperpolarized by these methods, as the fast reheating after polarization might disrupt the structure of these biomolecules.

In this work we have assumed diamonds with natural ^{13}C abundance (1.1%) which would already lead to a considerable signal enhancement in MRI applications. It is possible however to apply our scheme to diamonds with higher ^{13}C concentrations as the polarization transfer from electron to nuclear spin is not significantly affected by the presence of

^{13}C very close to the NV. A higher ^{13}C concentration will be beneficial however as the increase in the internuclear dipolar interaction leads to more effective polarization diffusion and hence a faster nuclear-spin polarization. The same effect will however lead to a reduction of the polarization lifetime as the faster diffusion allows polarization loss on the nanodiamond surface to diffuse more rapidly to the bulk. The latter shows that surface treatment of ^{13}C isotope enriched nanodiamonds can be expected to be particularly beneficial.

VIII. CONCLUSION

In conclusion, in the high magnetic field limit, we propose a scheme achieving macroscopic levels of ^{13}C nuclear-spin polarization in randomly oriented ensembles of nanodiamonds, realized as powder or solutions. To address the lack of a common natural quantization axis for the NV centers, an off-resonant microwave drive realizes a resonant double quantum transition and this, together with the integrated solid effect, enables microwave coupling and control of NV spins whose orientation deviates from the external magnetic field by less than 20°. Matching the effective Rabi frequency of the off-resonant double quantum transition of the NV centers to the nuclear-spin Larmor frequency enables near resonant coupling between NV electron spins and the nuclear spins, and the transfer of polarization from the initialized NV spins to the neighboring ^{13}C nuclear spins. Additionally, the effect of nuclear dipole-dipole interactions allows the weakly coupled nuclear spins to be polarized by spin diffusion. Adiabatic rotation (of the magnetic field or sample) can then extend the polarizing scheme to more NV spins, achieving a net polarization of all nuclear spins via our scheme. By using our polarization scheme, room-temperature, optical based polarization of the nuclear spins is made possible.

These results introduce several exciting opportunities for the application of hyperpolarized nanodiamonds, especially in the biomedical sciences. Diamond nanoparticles are biocompatible, exhibit no *in vivo* toxicity [49], and can be attached to a wide range of specific proteins, peptides, or antibodies [17] while maintaining long $T1$ times. Thus, hyperpolarized nanodiamonds present an exciting platform as MRI probes for molecular imaging. Finally, we would like to stress that the techniques that we have presented here for overcoming the random orientation and large zero-field splitting of NV centers in nanodiamonds apply more widely to color centers in any type of material that possesses an electron spin $S = 1$ in the ground state and admit optical pumping of this electron spin such as silicon divacancies in silicon-carbide and defect centers in quartz or silicon nanoparticles.

ACKNOWLEDGMENTS

We acknowledge helpful discussions with B. Luy, J. M. Cai, and Z. Y. Wang. This work was supported by the ERC Synergy grant BioQ, the EU projects DIADEMS, EQUAM, and SIQS, the Marie Curie Career Integration Grant (CIG) IonQuanSense (Grant No. 321798), the Niedersachsen-Israeli Research Cooperation Program, the Israel Science Foundation (Grant No. 1500/13), and an Alexander von Humboldt Professorship.

APPENDIX: EFFECTIVE HAMILTONIAN OF AN NV CENTER AT THE HIGH MAGNETIC FIELD LIMIT

In our work we assume that in the laboratory frame of reference a strong magnetic field is applied along the z direction, $\gamma_e B_z \gg D$. In the following we derive the representation of the NV center Hamiltonian Eq. (3) in the laboratory frame of coordinates. To this end we need to transform the zero-field splitting tensor, which is diagonal in the natural coordinate system defined by the NV center axes, to the laboratory frame of reference. We assume that the angle between the magnetic field, i.e., the z direction, and the NV axis, the z_θ direction, is given by θ and that the angle between the laboratory frame, y direction, and the NV center, y_θ directions, is given by ϕ in the x-y plane, as shown in Fig. 12. The spin operators in the NV system of coordinates, S_{x_θ}, S_{y_θ}, and S_{z_θ}, are then related to the spin operators S_x, S_y, and S_z in the laboratory coordinates by

$$\begin{aligned} S_{x_\theta} &= \sin\theta S_z + \cos\theta(\cos\phi S_x - \sin\phi S_y), \\ S_{y_\theta} &= \cos\phi S_y + \sin\phi S_x, \\ S_{z_\theta} &= \cos\theta S_z - \sin\theta(\cos\phi S_x - \sin\phi S_y). \end{aligned}$$

The Hamiltonian of the electron spin,

$$\begin{aligned} H_N^e = &\left(-\tfrac{1}{3}D + E\right)S_{x_\theta}S_{x_\theta} + \left(-\tfrac{1}{3}D - E\right)S_{y_\theta}S_{y_\theta} \\ &+ \left(\tfrac{2}{3}D\right)S_{z_\theta}S_{z_\theta} + \gamma_e B S_z, \end{aligned}$$

can then be rewritten in the basis defined by the eigenstates of the S_z operator of the electron spin, $\{|+1\rangle, |0\rangle, |-1\rangle\}$, as

$$H''_{NV} = \begin{pmatrix} D(\theta) + \gamma_e B_z & -G_1 & G_2 \\ -G_1^* & 0 & G_1 \\ G_2^* & G_1^* & D(\theta) - \gamma_e B_z \end{pmatrix}$$

with

$$\begin{aligned} D(\theta) &= \frac{D[1 + 3\cos(2\theta)] + 3E[1 - \cos(2\theta)]}{4}, \\ G_1 &= \frac{(D - E)\sin\theta\cos\theta e^{i\phi}}{\sqrt{2}}, \\ G_2 &= \frac{[D + 3E + (E - D)\cos 2\theta]e^{2i\phi}}{4}. \end{aligned}$$

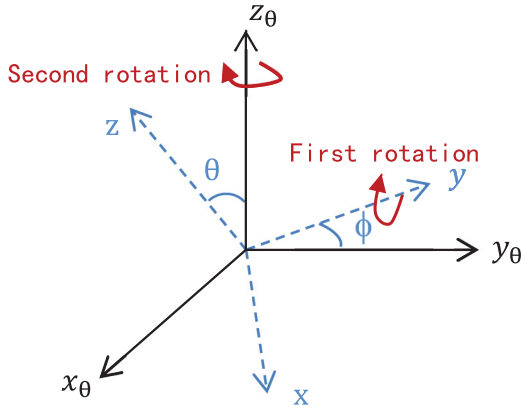

FIG. 12. (Color online) Two related rotations of the coordinate system are used to map from the natural orientation z_θ axis of the NV spin to z axis which is defined by the high magnetic field.

There exist two uncontrollable components, the angles θ and ϕ as well as the local strain E, which modifies the spin level structure.

As we know, a high magnetic field suppresses the effect of the off-diagonal terms in H''_{NV}. Assume that the Hamiltonian is of the form $H''_{NV} = H''_{NV0} + \epsilon V$, where H''_{NV0} is the diagonal part of the Hamiltonian and ϵV is the off-diagonal part. In our case the magnetic field is sufficiently large for us to assume that the off-diagonal part is a weak perturbation. By using the Schrieffer-Wolff transformation in condensed matter, the second-order corrections due to the off-diagonal terms ϵV can be obtained as

$$\langle\alpha|H''_M|\beta\rangle = \frac{\epsilon^2}{2}\left(\frac{\langle\alpha|V|i\rangle\langle i|V|\beta\rangle}{E_\alpha - E_i} - \frac{\langle\alpha|V|i\rangle\langle i|V|\beta\rangle}{E_i - E_\beta}\right),$$

in which H''_M is defined as the corrected Hamiltonian. By simple calculation, we find

$$\langle+1|H''_M|+1\rangle = \frac{|G_1|^2}{\gamma_e B + D(\theta)} + \frac{|G_2|^2}{2\gamma_e B},$$

$$\langle-1|H''_M|-1\rangle = \frac{|G_1|^2}{-\gamma_e B + D(\theta)} - \frac{|G_2|^2}{2\gamma_e B}.$$

After shifting the zero of energy, the effective Hamiltonian in the laboratory frame is given by

$$H''_{\text{eff}} = \gamma_e B S_z + D(\theta) S_z^2 + \delta(\theta) S_z,$$

in which

$$\delta(\theta) = \frac{\gamma_e B |G_1|^2}{(\gamma_e B)^2 - [D(\theta)]^2} + \frac{|G_2|^2}{2\gamma_e B}.$$

Therefore a strong magnetic field suppresses the first-order effect of the off-diagonal terms in H''_{NV} but results in a second-order modification of the diagonal elements $\delta(\theta)$. This is the Hamitonian as in Eq. (3).

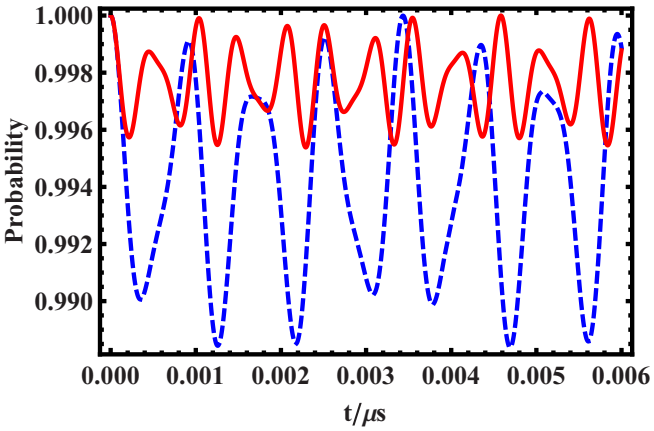

FIG. 13. (Color online) Validation of neglecting off-resonant coupling with $D = (2\pi)2870$ MHz, $\theta = 10^\circ$, $E = (2\pi)20$ MHz. The dashed blue line and solid red line present the time evolutions of the probability of the state $|0\rangle$ corresponding to $B = 0.36$ T and $B = 0.54$ T, respectively.

In order to estimate the validity of this approximation in the high magnetic field limit we have prepared the system in the state $|m_s = 0\rangle$ and observed the subsequent time evolution of its population under Hamiltonian H''_N in Fig. 13 (see caption for simulation parameters). It is evident that the population of the initial state $m_s = 0$ remains essentially constant which implies in turn that the effect of the off-diagonal elements in Hamiltonian H''_{NV} are indeed negligible for the moderate to high magnetic field case that is relevant to our work.

[1] F. Bloch, W. W. Hansen, and M. Packard, The nuclear induction experiment, Phys. Rev. **70**, 474 (1946).

[2] E. M. Purcell, H. C. Torrey, and R. V. Pound, Resonance absorption by nuclear magnetic moments in a solid, Phys. Rev. **69**, 37 (1946).

[3] S. Månsson, E. Johansson, P. Magnusson, C.-M. Chai, G. Hansson, J. S. Petersson, F. Ståhlberg, and K. Golman, ^{13}C imaging—a new diagnostic platform, Eur. J. Radiol. **16**, 57 (2006).

[4] P. C. Lauterbur, Image formation by induced local interactions: Examples employing nuclear magnetic resonance, Nature (London) **242**, 190 (1973).

[5] P. Dutta, A. Le, D. L. Vander Jagt, T. Tsukamoto, G. V. Martinez, C. V. Dang, and R. J. Gillies, Evaluation of LDH-A and glutaminase inhibition in vivo by hyperpolarised ^{13}C-pyruvate magnetic resonance spectroscopy of tumors, Cancer Res. **73**, 4190 (2013).

[6] F. A. Gallagher, M. I. Kettunen, D.-E. Hu, P. R. Jensen, M. Karlsson, A. Gisselsson, S. K. Nelson, T. H. Witney, S. E. Bohndiek, G. Hansson *et al.*, Production of hyperpolarised [1, 4-^{13}C$_2$] malate from [1, 4-^{13}C$_2$] fumarate is a marker of cell necrosis and treatment response in tumors, Proc. Natl. Acad. Sci. USA **106**, 19801 (2009).

[7] F. A. Gallagher, M. I. Kettunen, S. E. Day, D.-E. Hu, J. H. Ardenkjær-Larsen, P. R. Jensen, M. Karlsson, K. Golman, M. H. Lerche, K. M. Brindle *et al.*, Magnetic resonance imaging of pH in vivo using hyperpolarised ^{13}C-labelled bicarbonate, Nature (London) **453**, 940 (2008).

[8] J. H. Ardenkjær-Larsen, B. Fridlund, A. Gram, G. Hansson, L. Hansson, M. H. Lerche, R. Servin, M. Thaning, and K. Golman, Increase in signal-to-noise ratio of $>10,000$ times in liquid-state NMR, Proc. Natl. Acad. Sci. USA **100**, 10158 (2003).

[9] K. Golman, M. Thaning *et al.*, Real-time metabolic imaging, Proc. Natl. Acad. Sci. USA **103**, 11270 (2006).

[10] C.-G. Joo, K.-N. Hu, J. A. Bryant, and R. G. Griffin, In situ temperature jump high-frequency dynamic nuclear polarization experiments: Enhanced sensitivity in liquid-state NMR spectroscopy, J. Am. Chem. Soc. **128**, 9428 (2006).

[11] S. Bowen and C. Hilty, Time-resolved dynamic nuclear polarization enhanced NMR spectroscopy, Angew. Chem. **120**, 5313 (2008).

[12] J. Leggett, R. Hunter, J. Granwehr, R. Panek, A. J. Perez-Linde, A. J. Horsewill, J. McMaster, G. Smith, and W. Köckenberger, A dedicated spectrometer for dissolution DNP NMR spectroscopy, Phys. Chem. Chem. Phys. **12**, 5883 (2010).

[13] Q. A. Pankhurst, J. Connolly, S. Jones, and J. Dobson, Applications of magnetic nanoparticles in biomedicine, J. Phys. D **36**, R167 (2003).

[14] J. W. Aptekar, M. C. Cassidy, A. C. Johnson, R. A. Barton, M. Lee, A. C. Ogier, C. Vo, M. N. Anahtar, Y. Ren, S. N. Bhatia *et al.*, Silicon nanoparticles as hyperpolarised magnetic resonance imaging agents, ACS Nano **3**, 4003 (2009).

[15] P. Dutta, G. V. Martinez, and R. J. Gillies, Nanodiamond as a new hyperpolarizing agent and its ^{13}C MRS, J. Phys. Chem. Lett. **5**, 597 (2014).

[16] E. Rej, T. Gaebel, T. Boele, D. E. Waddington, and D. J. Reilly, Hyperpolarised nanodiamond with long spin relaxation times, Nat. Commun. **6**, 8459 (2015).

[17] V. N. Mochalin, O. Shenderova, D. Ho, and Y. Gogotsi, The properties and applications of nanodiamonds, Nat. Nanotechnol. **7**, 11 (2012).

[18] L. B. Casabianca, A. I. Shames, A. M. Panich, O. Shenderova, and L. Frydman, Factors affecting DNP NMR in polycrystalline diamond samples, J. Phys. Chem. C **115**, 19041 (2011).

[19] F. Jelezko, T. Gaebel, I. Popa, M. Domhan, A. Gruber, and J. Wrachtrup, Observation of Coherent Oscillation of a Single Nuclear Spin and Realisation of a Two-Qubit Conditional Quantum Gate, Phys. Rev. Lett. **93**, 130501 (2004).

[20] M. G. Dutt, L. Childress, L. Jiang, E. Togan, J. Maze, F. Jelezko, A. Zibrov, P. Hemmer, and M. Lukin, Quantum register based on individual electronic and nuclear spin qubits in diamond, Science **316**, 1312 (2007).

[21] V. Jacques, P. Neumann, J. Beck, M. Markham, D. Twitchen, J. Meijer, F. Kaiser, G. Balasubramanian, F. Jelezko, and J. Wrachtrup, Dynamic Polarization of Single Nuclear Spins by Optical Pumping of Nitrogen-Vacancy Color Centers in Diamond at Room Temperature, Phys. Rev. Lett. **102**, 057403 (2009).

[22] P. Neumann, J. Beck, M. Steiner, F. Rempp, H. Fedder, P. R. Hemmer, J. Wrachtrup, and F. Jelezko, Single-shot readout of a single nuclear spin, Science **329**, 542 (2010).

[23] J. P. King, P. J. Coles, and J. A. Reimer, Optical polarization of ^{13}C nuclei in diamond through nitrogen vacancy centers, Phys. Rev. B **81**, 073201 (2010).

[24] P. London, J. Scheuer, J.-M. Cai, I. Schwarz, A. Retzker, M. B. Plenio, M. Katagiri, T. Teraji, S. Koizumi, J. Isoya *et al.*, Detecting and Polarizing Nuclear Spins with Double Resonance on a Single Electron Spin, Phys. Rev. Lett. **111**, 067601 (2013).

[25] E. Togan, Y. Chu, A. Imamoglu, and M. Lukin, Laser cooling and real-time measurement of the nuclear spin environment of a solid-state qubit, Nature (London) **478**, 497 (2011).

[26] H.-J. Wang, C. S. Shin, C. E. Avalos, S. J. Seltzer, D. Budker, A. Pines, and V. S. Bajaj, Sensitive magnetic control of ensemble nuclear spin hyperpolarisation in diamond, Nat. Commun. **4**, 1940 (2013).

[27] G. A. Álvarez, C. O. Bretschneider, R. Fischer, P. London, H. Kanda, S. Onoda, J. Isoya, D. Gershoni, and L. Frydman, Local and bulk ^{13}C hyperpolarization in nitrogen-vacancy-centered diamonds at variable fields and orientations, Nat. Commun. **6**, 8456 (2015).

[28] R. Fischer, C. O. Bretschneider, P. London, D. Budker, D. Gershoni, and L. Frydman, Bulk Nuclear Polarization Enhanced at Room Temperature by Optical Pumping, Phys. Rev. Lett. **111**, 057601 (2013).

[29] S. Hartmann and E. Hahn, Nuclear double resonance in the rotating frame, Phys. Rev. **128**, 2042 (1962).

[30] J. Cai, F. Jelezko, M. B. Plenio, and A. Retzker, Diamond-based single-molecule magnetic resonance spectroscopy, New J. Phys. **15**, 013020 (2013).

[31] J. Cai, B. Naydenov, R. Pfeiffer, L. P. McGuinness, K. D. Jahnke, F. Jelezko, M. B. Plenio, and A. Retzker, Robust dynamical decoupling with concatenated continuous driving, New J. Phys. **14**, 113023 (2012).

[32] J. Cai, A. Retzker, F. Jelezko, and M. B. Plenio, A large-scale quantum simulator on a diamond surface at room temperature, Nat. Phys. **9**, 168 (2013).

[33] The components of $\vec{S} = S_x\vec{e}_x + S_y\vec{e}_y + S_z\vec{e}_z$ are given by $S_x = \frac{1}{\sqrt{2}}\begin{pmatrix}0&1&0\\1&0&1\\0&1&0\end{pmatrix}$, $S_y = \frac{1}{\sqrt{2}}\begin{pmatrix}0&-i&0\\i&0&-i\\0&i&0\end{pmatrix}$, $S_z = \begin{pmatrix}1&0&0\\0&0&0\\0&0&-1\end{pmatrix}$.

[34] A. Henstra, P. Dirksen, and W. T. Wenckebach, Enhanced dynamic nuclear polarization by the integrated solid effect, Phys. Lett. A **134**, 134 (1988).

[35] C. Zener, Non-adiabatic crossing of energy levels, in *Proceedings of the Royal Society of London A: Mathematical, Physical and Engineering Sciences* No. 833 (The Royal Society, London, 1932), Vol. 137, pp. 696–702.

[36] A. Henstra, T.-S. Lin, J. Schmidt, and W. T. Wenckebach, High dynamic nuclear polarization at room temperature, Chem. Phys. Lett. **165**, 6 (1990).

[37] A. Henstra and W. T. Wenckebach, Dynamic nuclear polarization via the integrated solid effect I: theory, Mol. Phys. **112**, 1761 (2014).

[38] T. Eichhorn, B. v. d. Brandt, P. Hautle, A. Henstra, and W. T. Wenckebach, Dynamic nuclear polarization via the integrated solid effect II: experiments on naphthalene-h_8 doped with pentacene-d_{14}, Mol. Phys. **112**, 1773 (2014).

[39] A. Laraoui and C. A. Meriles, Approach to dark spin cooling in a diamond nanocrystal, ACS Nano **7**, 3403 (2013).

[40] J. Frenkel, *Kinetic Theory of Liquids* (Dover Publications, New York, 1955).

[41] A. Ermakova, G. Pramanik, J.-M. Cai, G. Algara-Siller, U. Kaiser, T. Weil, Y.-K. Tzeng, H. Chang, L. McGuinness, M. B. Plenio *et al.*, Detection of a few metallo-protein molecules using color centers in nanodiamonds, Nano Lett. **13**, 3305 (2013).

[42] H. Christ, J. I. Cirac, and G. Giedke, Quantum description of nuclear spin cooling in a quantum dot, Phys. Rev. B **75**, 155324 (2007).

[43] A. M. Panich, N. A. Sergeev, A. I. Shames, V. Yu. Osipov, J. P. Boudou, and S. D. Goren, Size dependence of ^{13}C nuclear spin-lattice relaxation in micro-and nanodiamonds, J. Phys.: Condens. Matter **27**, 072203 (2015).

[44] M. Kaviani, P. Deak, B. Aradi, T. Frauenheim, J. P. Chou, and A. Gali, Proper surface termination for luminescent near-surface NV centers in diamond, Nano Lett. **14**, 4772 (2014).

[45] A. Krueger, New carbon materials: Biological applications of functionalized nanodiamond materials, Chem. Eur. J. **14**, 1382 (2008).

[46] C. Belthangady, N. Bar-Gill, L. M. Pham, K. Arai, D. Le Sage, P. Cappellaro, and R. L. Walsworth, Dressed-State Resonant Coupling Between Bright and Dark Spins in Diamond, Phys. Rev. Lett. **110**, 157601 (2013).

[47] L.-J. Su, C.-Y. Fang, Y.-T. Chang, K.-M. Chen, Y.-C. Yu, J.-H. Hsu, and H.-C. Chang, Creation of high density ensembles of

nitrogen-vacancy centers in nitrogen-rich type Ib nanodiamonds, Nanotechnology **24**, 315702 (2013).

[48] A spherical shaped nanodiamond of diameter 30 nm has the volume $3.21 \times 10^{-17}\text{cm}^3$. Each unit cell of the diamond crystal has the volume $4.49 \times 10^{-23}\,\text{cm}^3$; the number of unit cells in the given particle is 7.14×10^6. Eight carbon atoms per unit cell of diamond crystal gives the total number of carbon atom 5.71×10^7. Natural abundance of the ^{13}C 1.1% leads to the total number of ^{13}C nuclear spin in a 30-nm nanodiamond of 2.29×10^5.

[49] Y. Zhu, J. Li, W. Li, Y. Zhang, X. Yang, N. Chen, Y. Sun, Y. Zhao, C. Fan, and Q. Huang, The biocompatibility of nanodiamonds and their application in drug delivery systems, Theranostics **2**, 302 (2012).